UNIVERSIDADE DE LISBOA
FACULDADE DE CIÊNCIAS
DEPARTAMENTO DE FÍSICA

Magnetic calculations: from atomic to nano-scale

Rafael Martinho Vieira

Mestrado em Física
Física da Matéria Condensada e Nano-Materiais

Dissertação orientada por:
Prof. Doutor Thomas Gasche
Prof^{a}. Doutora Maria Margarida Cruz

2017

Acknowledgments

Foremost, I would like to thank my supervisor Prof. Dr. Thomas Gasche, and my co-supervisor Prof. Dr. Margarida Cruz for their patience, guidance, availability and for giving me the opportunity and support to work on this subject as my master thesis. Also, I would like to thank the MagNano group for the provided resources.

A special thank to Prof. Dr. Manuel Ritcher of IFW Dresden for guiding me through the ways of the DFT calculations, as well to IFW for providing the computational resources required for the computations.

Likewise, I would like to praise the Erasmus exchange program and to thank the respective grant for giving me the lifetime opportunity of studying and training abroad (more precisely on Dresden). I thank Prof. Dr. Guiomar Evans for the help through the bureaucratic complications that unfortunately always appear in this kind of enterprise. A huge thanks to all the new made multiCooltural friends for sharing with me this experience and for warming the cold german winter.

A tremendous thanks to my supercalifragilisticexpialidocious friends Carolina, Isabel and Ana for sharing this long journey and for being like a family in a city where I have none. Thanks, Vitorino for all advice given, even if stubbornly I choose to ignore some of them. You all make it possible to happen.

A special thanks to my parents, for always being here supporting me and for making it possible to me to reach this far.

Last but not least, thanks to the Pinhons, to my colleagues, and to all my friends for helping me during this phase of my life and for making me smile, like you always do!

Abstract

Recently there as been a rising interest in using magnetic nanoparticles as a heat source for tumour therapy and also in thermal activated drug delivery, in a technique known as magnetic hyperthermia. Due to their biocompatibility and magnetic properties, iron oxides, as magnetite, have been considered promising materials for this technique.

The coercivity of magnetic materials is an important parameter in magnetic hyperthermia providing a measure of the heat provided by the magnetic system. In this work, the coercivity of single nanoparticles is computed for structures with different geometry/composition using micromagnetic simulations. Ten ellipsoids of revolution with different major/minor axis ratio c/a ranging from 0.85 to 2.00 were considered. Also, four mix composed spherical structures of magnetite and maghemite with volume ratio ranging from 0.65 to 1.00 were simulated to evaluate the oxidation effect on the magnetic hyperthermia performance. The nanoparticle's volume relevance was tested by comparing the results for three spherical structures, with the radius ranging from 7.5 to 13 nm.

Most of the material parameters on which the micromagnetic simulations in this work depend upon were computed in advance through DFT calculations. The LDA+U method was explored as a possible improvement for the magnetite magnetic parameters calculation although there is no clear improvement in the results. Additionally, for a magnetite crystal, the magnetic parameters dependence with the lattice parameters were studied through the application of an uniaxial strain. In this study were considered nine crystalline structures under a lateral strain, ranging from -3% to 3%. The obtained results shows little sensitivity of the system to small strains, in the sense that it does not induce an alteration of the magnetic behaviour.

The results obtained from the micromagnetic simulations show less sensitivity of the nanoparticles performance to small axis ratio variations in the elongated structures with coercivity comparable with the sphere structure. Also, the results show that oxidation effects have a minor influence on the nanoparticles performance in magnetic hyperthermia. As expected for the range of variation considered, variations on the structure's volume were found not relevant for the magnetic properties of the system.

Key Words:

DFT, Micromagnetism, Magnetite, Maghemite, Magnetic hyperthermia

Resumo

Recentemente tem havido um crescente interesse na utilização clínica de hipertermia magnética, como terapia para tratamento de tumores ou para administração de fármacos. Nesta técnica, nanopartículas magnéticas sob aplicação de um campo magnético externo alterno são utilizadas como fonte de calor. O calor libertado está associado ao trabalho realizado pelo campo externo na inversão da magnetização das nanopartículas e é proporcional à coercividade do sistema. A coercividade magnética é uma grandeza que quantifica a resistência de um sistema magnético à desmagnetização do mesmo. A geometria e composição dos sistemas magnéticos possuem um enorme impacto na coercividade dos mesmos, sendo importante compreender a influência destes parâmetros na coercividade.

Pela sua biocompatibilidade e devido às suas propriedades magnéticas, óxidos de ferro como a magnetite estão entre os mais promissores materiais para aplicação terapêutica da hipertermia magnética. A magnetite é um material ferrimagnético descrito por uma rede cristalina fcc constituída por iões de ferro e oxigénio. Por oxidação a magnetite é susceptível de transformar-se em maghemite, um material que partilha as mesmas propriedades magnéticas. Quando descrita por uma rede cúbica a maghemite pode ser tratada como magnetite com deficiência de ferro (ou excesso de oxigénio). Neste trabalho foram calculados inicialmente, via DFT (escala atómica), os parâmetros necessários para descrever nanopartículas magnéticas de magnetite e /ou maghemite à escala nano com recurso à teoria micromagnética. Posteriormente foram realizadas simulações dinâmicas para estruturas elipsoidais com a recurso à equação de Landau-Lifshitz-Gilbert de forma a obter uma medida de coercividade para estas estruturas.

Para a realização dos cálculos em DFT o código *FPLO* foi utilizado. A presença de electrões de valência $3d$ na estrutura cristalina dos compostos indicia que será melhor a utilização de LDA+U, um método eficaz no tratamento de electrões correlacionados. De forma a averiguar a eficácia do referido método no cálculo dos parâmetros pretendidos, o potencial efectivo U foi variado entre 0 e 7 eV para quatro simulações da estrutura cúbica da magnetite. Observou-se que o método não traz benefícios no cálculo do momento magnético do sistema e tende a diminuir o valor da constante de anisotropia cúbica (K_1), o que pode acrescentar dificuldades no cálculo desta constante, caracteristicamente difícil de determinar devido ao seu diminuto valor. No entanto, este método permitiu a convergência do sistema para uma fase ferromagnética, permitindo fazer uma aproximação da constante de troca (J) via modelo Ising. Verifica-se que o valor desta constante se aproxima mais da estimativa teórica no quadro da teoria de campo médio, para o potencial efectivo de 4.5 eV.

A dependência do momento magnético, de J e K_1 com os parâmetros de rede a volume constante foi estudada através da imposição de tensão uniaxial na estrutura de magnetite. Para tal, foram consideradas nove estruturas com tensão lateral entre -3% e 3%, e no cálculo de J foi utilizado o método LDA+U com o potencial efectivo de 4.5 eV. Nos resultados obtidos verifica-se pouca sensibilidade do momento magnético e K_1 para as variações consideradas nos parâmetros de rede, no último as variações observadas não alteram nem o sinal nem a ordem de grandeza do parâmetro. A constante de troca revelou-se mais sensível às alterações na rede cristalina sem, no entanto, haver alterações que induzam mudanças no

comportamento magnético das estruturas nanométricas a considerar. A deformação da rede por aplicação da tensão uniaxial reduz a simetria da rede cristalina tendo sido necessária a construção de uma rede tetragonal para a descrição das estruturas sob tensão. Ao comparar os valores calculados para K_1, J e M_s na rede cúbica e na rede tetragonal sem tensão aplicada verifica-se que existe coerência dos cálculos sendo os resultados coincidentes. Para K_1, o valor obtido para as duas estruturas é próximo de valores publicados em cálculos semelhantes.

A impossibilidade de usar a descrição cúbica para a maghemite no código utilizado para os cálculos em DFT, implicou a necessidade de utilizar uma rede cristalina com menor simetria, implicando um cálculo numericamente mais exigente. Não foi possível convergir o cálculo de K_1 para esta estrutura, tendo sido obtidos apenas os parâmetros M_s e uma estimativa para J. Foram realizadas várias tentativas de relaxar uma estrutura com uma proporção de átomos ferro/oxigénio intermédia entre a magnetite e a maghemite mas sem sucesso, impedindo determinar a dependência deste parâmetro com a deficiência de ferro do composto. Relativamente a M_s, a relação entre os valores para os dois compostos é a esperada, tendo a maghemite um menor momento magnético por fórmula unitária. Este resultado é coerente com o défice de iões de ferro neste último composto. Uma vez que o défice engloba apenas os iões de ferro de uma das sub-redes ferrimagnéticas, o desequilíbrio entre as sub-redes é reduzido, conduzindo a um menor momento magnético total.

Para a realização das simulações em micromagnetismo o software *MagPar* foi utilizado enquanto que a modelação geométrica das malhas foi efectuada previamente no software *Gmsh*. Uma vez que o sistema em estudo é de uma única nanopartícula com um único domínio magnético a definição clássica de coercividade magnética não é aplicável, no entanto uma medida de coercividade pode ser obtida pelo campo de nucleação (H_n) definido como o campo externo aplicado para qual é iniciada a inversão da magnetização do sistema.

A dependência de H_n com o rácio entre os eixos maior/menor em elipsoides de revolução foi analisada para dez geometrias com rácios entre os 0.85 (geometria achatada) e 2.00 (geometria alongada). É observado que tanto para H_n, como a para a direcção de magnetização para o sistema relaxado, existe dependência com a geometria utilizada. Verifica-se para o caso esférico que o valor de H_n é um máximo local, o que pode ter como consequência uma diminuição no desempenho das nanopartículas na hipertermia magnética para pequenas variações/defeitos nas nanoestruturas. Verifica-se também para geometrias com o rácio entre os eixos do elipsoide próximo de 1.00 (caso esférico), a existência de um desvio na magnetização antes da inversão, que leva à redução do calor libertado pelas nanopartículas, durante a inversão da magnetização por aplicação de um campo externo. Conjuntamente, foram identificadas geometrias mais alongadas com H_n semelhante ao da esfera como escolhas mais apropriadas para as nanopartículas.

Devido à oxidação, não é incomum a presença de uma camada de maghemite em nanopartículas de magnetite. Para analisar o impacto da oxidação no desempenho das nanopartículas foram simuladas quatro estruturas esféricas de igual volume compostas por núcleo de magnetite e uma camada de maghemite. As proporções entre os dois constituintes foram variadas tendo sido o rácio de volumes alterado entre 1.00 e 0.65 (magnetite maioritária). Os resultados obtidos indicam um fraco impacto da oxidação no campo de nucleação e consequentemente no desempenho das nanopartículas, havendo a diminuta diferença de 6 kAm para H_n entre uma esfera totalmente composta por magnetite e uma esfera composta por iguais proporções de magnetite e maghemite.

Enquanto a dimensão das nanopartículas consideradas for inferior ao limite critico para existência, apenas de um domínio magnético, não deverá haver alteração no seu comportamento para variações de volume. De forma a testar se esta característica é verificada e para comparar o desempenho entre

os dois tipos de malhas geradas, foram realizadas e comparadas simulações para três esferas de raios compreendidos entre 7.5 e 13 nm. Como esperado, não foi verificada nenhuma influência do volume no cálculo do campo de nucleação (dentro da incerteza associada).

Palavras-chave:

DFT, Micromagnetismo, Magnetite, Maghemite, Hipertermia magnética

Contents

List of Figures

List of Tables

List of Abbreviations

BZ	Brillouin Zone
DFT	Density Functional Theory
DOS	Density Of States
FPLO	Full-Potential Local-Orbital
fu	formula unit
GGA	Generalized Gradient Approximation
LDA	Local Density Approximation
LLG	Landau-Lifshitz-Gilbert
MAE	Magnetocrystalline Anisotropy
uc	unit cell

Chapter 1

Introduction

Recently there has been a rising interest in using magnetic hyperthermia for tumour therapy [1][2]. This technique is based on the fact that magnetic nanoparticles release heat when placed in an alternating magnetic field.

In this work nanoparticles of iron oxide are addressed due to their biocompatibility and magnetic properties. Magnetite (Fe_3O_4) is one of these oxides, and it is susceptible to oxidation, becoming maghemite ($\gamma - Fe_2O_3$) through this process, an oxide that has similar magnetic properties and is also suitable for magnetic heating. It is not uncommon the presence of an oxidized layer at the surface of magnetite nanoparticles [3].

At room temperature, the crystalline structure of magnetite can be described as an fcc structure defined by the oxygen anions, with the cations Fe^{3+} occupying the tetrahedral sites (A) along with a mixture of Fe^{2+} and Fe^{3+} at octahedral sites (B). Maghemite can be described with a similar crystalline structure if $\frac{1}{6}$ of the B sites are considered to be empty, and on this perspective maghemite could be seen as magnetite with iron deficiency. Both compounds are ferrimagnetic resulting from the antiferromagnetic coupling between Fe_A and Fe_B mediated by the oxygen ions, presenting magnetic moment even in absence of an applied field and a magnetic structure with domains.

Ferrimagnetic materials usually present hysteresis in the magnetization dependence of the external applied field. When a system presents magnetic hysteresis, the area enclosed within the hysteresis loop represents the irreversible work done by the magnetic forces, dissipated in the system as heat. To be used in tumour therapy as heat source to damage cancer cells, it is important to maximize the magnetic nanoparticle heating power in order to have the required energy with reduced particle dosage.

The coercivity of magnetic materials is defined as the reverse field needed to demagnetize the sample after being saturated. The bigger is coercivity, the larger is the hysteresis loop and so more heat is provided from the magnetic system. Small nanoparticles are in general single domain particles. For these particles the coercivity is related with the energy barrier between easy magnetization orientations and it depends strongly on their geometry and composition. It is then of major importance to understand how variations in these parameters affect the coercive field, in order to optimize the magnetic hysteresis energy losses. For a single magnetic nanoparticle the coercive field is not a good parameter to determine since magnetization reversal has no intermediate state of zero magnetization (component parallel to the applied field). Therefore, the field for which the magnetization reversion just starts, also known as nucleation field (H_n), is used as a measure of the coercivity

To study the magnetic energy dissipated by the nanoparticles and their dependence on the geometry and composition, hysteresis loops were simulated using micromagnetic theory. The effects of shape variation with constant volume were studied using ellipsoids of revolution with different major/minor

axis ratio, and the influence of composition variation due to superficial oxidization was studied using spherical nanoparticles constant volume. The nanoparticles dimensions are within the nanometre range, making necessary to perform nano-scale calculations in order to correctly describe these systems.

The parameters upon which micromagnetism simulations depend, are the magnetization of saturation (M_s), the exchange constant (J) and the anisotropy constants (K_1 and K_2) which determinations require calculations at the atomic scale. The Density Functional Theory (DFT) is a very successful and widely used method to compute the electronic structure of many body systems which range from atoms via small nano-structures to extended periodic systems. This method is an essential tool in Solid State Physics and Chemistry due to the wide applications and properties that can be evaluated. DFT calculations were done for stoichiometric magnetite and maghemite crystals relaxed and under stress (for the magnetite case) in order to determine the parameters required for the micromagnetic calculations.

This dissertation is essentially divided in two parts related with the scale addressed by the calculations, the atomic scale and the nano-scale. In the first part, the performed DFT simulations are discussed and the obtained results presented and compared with similar calculations. The second part concerns micromagnetic calculations. The theoretical fundamentals of each method and the related magnetic concepts are also introduced in the two parts. The text ends with the main conclusions of this work.

Chapter 2

DFT Calculations

2.1 Introduction

2.1.1 Magnetic Concepts I

Exchange Energy

In a quantum system electrons are indistinguishable fermions, being the exchange energy the energy associated with this symmetry. This can be illustrated with the simple system of two independent electron a and b. The two electron wave function, built with one electron wave functions, must be antisymmetric (Pauli principle) and invariant for the interchange of the electrons resulting in functions

$$\psi_S = \frac{1}{\sqrt{2}}[\phi_a(\vec{r}_1)\phi_b(\vec{r}_2) + \phi_a(\vec{r}_2)\phi_b(\vec{r}_1)]\chi_S \quad , \tag{2.1}$$

$$\psi_T = \frac{1}{\sqrt{2}}[\phi_a(\vec{r}_1)\phi_b(\vec{r}_2) - \phi_a(\vec{r}_2)\phi_b(\vec{r}_1)]\chi_T \quad , \tag{2.2}$$

where S stands for singlet state (total spin $S = 0$) corresponding to a symmetric spatial function and antisymmetric spin function $\frac{1}{2}(|\uparrow\downarrow\rangle - |\downarrow\uparrow\rangle)$, and T for a triplet state (total spin $S = 1$) with antisymmetric spatial function and symmetric spin functions $\frac{1}{2}(|\uparrow\downarrow\rangle + |\downarrow\uparrow\rangle), |\uparrow\uparrow\rangle, |\downarrow\downarrow\rangle$. Assuming there is no external applied field and that the spin components χ_S and χ_T are normalized, the energy difference between the two states is [4]

$$E_S - E_T = 2\int \phi_a^*(\vec{r}_1)\phi_b^*(\vec{r}_2)\hat{\mathscr{H}}\phi_a(\vec{r}_2)\phi_b(\vec{r}_1)\, d\vec{r}_1 d\vec{r}_2 \quad , \tag{2.3}$$

where $\hat{\mathscr{H}}$ is the Coulomb interaction operator. This integral defines the exchange constant J [1] as [4]

$$J = \frac{E_S - E_T}{2} \quad . \tag{2.4}$$

For a pair of coupled electrons the energy difference can be written in terms of the operator $\hat{S}_a.\hat{S}_b$. The spin operator has the same properties as the angular momentum operator, so $\hat{S}_a.\hat{S}_b = \frac{1}{2}\left[(\hat{S}_a + \hat{S}_b)^2 - \hat{S}_a{}^2 - \hat{S}_b{}^2\right]$ has eigenvalues $\frac{1}{4}$ ($S = 1$, triplet state) and $\frac{-3}{4}$ ($S = 0$, singlet state) allowing to write the exchange term of the Hamiltonian as

$$\hat{\mathscr{H}} = \frac{1}{4}(E_S + 3E_T) - (E_S - E_T)\hat{S}_a.\hat{S}_b \quad . \tag{2.5}$$

The first term can be discarded when studying the magnetic energy variation since it is a constant and can be absorbed in the zero energy redefinition, allowing to rewrite the exchange term in the Hamiltonian

[1] This definition is not universal in the magnetism literature, where can also be found J defined as twice this value.

Table 2.1: Directions of easy, medium and hard magnetization in a cubic crystal. Adapted from *Cullity et all*.

K_1	+	+	+	-	-	-
K_2	$[+\infty, -9K_1/4[$	$[-9K_1/4, -9K_1[$	$[-9K_1, -\infty[$	$[-\infty, 9K_1/4[$	$[9K_1/4, 9K_1[$	$[9K_1, +\infty[$
Easy	$<100>$	$<100>$	$<111>$	$<111>$	$<110>$	$<110>$
Medium	$<110>$	$<111>$	$<100>$	$<110>$	$<111>$	$<100>$
Hard	$<111>$	$<110>$	$<110>$	$<100>$	$<100>$	$<111>$

as

$$\hat{\mathscr{H}} = -2J\hat{S}_a.\hat{S}_b \quad . \tag{2.6}$$

The generalization of this interaction for a many body system is far from trivial, but assuming a lattice of fermions with only first neighbours interactions, the corresponding Hamiltonian can be written as the sum over all pair interactions

$$\hat{\mathscr{H}} = -\sum_{i,j} J_{ij}\hat{S}_i.\hat{S}_j \quad , \tag{2.7}$$

which is known as the Heisenberg Hamiltonian.

Magnetocrystalline Anisotropy Energy

The magnetization ($\vec{M} = (m_x, m_y, m_z)$) is defined as the volume density of the magnetic dipole moment, and characterizes the magnetic state of the system.

An important term to the magnetic energy is the magnetocrystalline anisotropy energy (MAE) that arises from the spin-orbit interaction and bonding states. The MAE reduces the energy for magnetization aligned along some crystallographic directions (easy magnetization axis), and increases the energy for others. This anisotropy energy is directly related to the crystal symmetry and is larger for low symmetry structures compared to more symmetric ones [4].

The magnetocrystalline energy density must reflect the crystalline structure symmetry. For a cubic crystal, case of the iron oxides studied, the cubic symmetry implies that the directions or planes obtained interchanging the Miller's indices are equivalent regardless sign, so only even terms in the magnetization components appear in the MAE. The lower order term which satisfies this conditions is of second order $m_x^2 + m_y^2 + m_z^2$. This term does not depend on the orientation, implying need of the fourth order terms to describe this dependence.

$$\varepsilon_{ani} = K_0 + K_1(m_x^2m_y^2 + m_x^2m_z^2 + m_y^2m_z^2) + K_2m_x^2m_y^2m_z^2 \quad , \tag{2.8}$$

expression equivalent to [5]

$$\varepsilon_{ani} = K_0 - \frac{K_1}{2}(m_x^4 + m_y^4 + m_z^4) + K_2m_x^2m_y^2m_z^2 \quad . \tag{2.9}$$

For the MAE evaluation the constant term can be dropped and therefore

$$E_{ani} = \int K_1(m_x^2m_y^2 + m_x^2m_z^2 + m_y^2m_z^2) + K_2m_x^2m_y^2m_z^2 \, dV \quad . \tag{2.10}$$

If K_2 is zero, the easy, medium and hard directions of magnetization are determined by the sign of K_1, but if K_2 is not zero they depend on both anisotropy constant values as shown on Table 2.1.

2.1.2 Density Functional Theory

Most of the characteristics displayed by atomic systems are intimately related with their electronic structures. Since even the most simple atomic structures are many-body systems, to solve their electronic structure is a remarkable problem.

The adiabatic principle states that a physical system in the ground state will remain all time in the ground state for a perturbation acting slowly, i.e the ground state is separated by a gap from the excitation spectrum [6]. This adiabatic principle simplifies the quantum mechanical treatment of adiabatic forces, in molecules and solids, allowing to decouple the motion equations of electrons and core due to the low electron to core mass ratio.

Using the adiabatic approximation, the Hamiltonian operator for a system with N interacting electrons, under an external potential can be written as

$$\hat{H} = \sum_{i=1}^{N} -\frac{\nabla_i^2}{2} + \sum_{\substack{i,j=1 \\ i\neq j}}^{N} \frac{1}{2} w(|\vec{r}_i - \vec{r}_j|) + \sum_{i=1}^{N} v(\vec{r}_i) \tag{2.11}$$

$$= \hat{T}_i + \hat{W} + \hat{v} \tag{2.12}$$

using the operators of Kinetic Energy ($\hat{T}$), Self-Interaction ($\hat{W}$, also known as Hartree energy), and External Potential ($\hat{v}$).

One successful and widely used method to solve these systems is the Density Functional Theory (DFT). Instead of solving a problem of $3N$ variables, DFT distinguishes itself by solving the system's Hamiltonian for the electron density, reducing this way the problem's dimensions from $3N$ to 3.

The logical basis of the DFT were established by Hohenberg, Kohn and Sham in the middle 60's, Walter Kohn and John Pople being awarded with the 1998 Nobel Prize in Chemistry for their contributions. Due the numerical simplification obtained by rewriting the Hamiltonian as density dependent, DFT popularity increased vastly and many developments emerged since then.

Hohenberg-Kohn Theory

Hohenberg and Kohn postulated two central theorems that form the DFT's basis. The first states that, for every given density $n(x)$, defined on the whole x-space, there is <u>*at most*</u> one potential function $v(x)\,mod(const)$ for which the given density is the ground state. Every functional with dependence on $v(x)$ can then be transformed into a functional with density dependence $v[n]$ [7]. The corresponding ground state, if exists, is gauge invariant for an added constant potential

$$E[v + const] = E[v] + N.const \quad . \tag{2.13}$$

The second theorem is a variational principle that states the existence of an energy functional of the density $E[n(x)]$, which is stationary with respect to variations of the ground state density

$$E[v] = min\{F_{HK}[n] + (n|v[n])\} \quad , \tag{2.14}$$

where $F_{HK}[n]$ is the Hohenberg-Kohn density functional.

The Levy-Lieb Theory

Although the Hohenberg-Kohn theory assumes that for every density n there exists a corresponding potential for which n is the ground-state density, without setting explicitly a class of densities n and

potentials v, not every density is v-representable. An extension of the Hohenberg-Kohn theory made by Levy-Lieb allows to overcome this problem requiring the densities to be N-representable, i.e. to be derived from an N-electron antisymmetric wavefunction.

The ground state assumption is alleviated when mixed states are allowed. For the Hamiltonian (2.11) the generic type of ensemble states can be admitted

$$\hat{\rho} = \sum_k |\psi_k\rangle \, p_k \, \langle\psi_k| \, , \; 0 \leq p_k \leq 1, \; \sum_k p_k = 1 \tag{2.15}$$

$\hat{\rho}$ being the density matrix operator of a N-particles mixed state, and $|\psi_k\rangle$ normalized N-particles pure states defined as combinations of orthonormal particle number eigenstates

$$|\psi_k\rangle = \sum_{L_k} c_{L_k} |\phi_{L_k}\rangle \, , \; \sum_{L_k} |c_{L_k}|^2 = 1, \; \hat{N}\,|\phi_{L_k}\rangle = |\phi_{L_k}\rangle \, L_k \quad , \tag{2.16}$$

with $L_k = \{l_1, ..., l_{N_k}\}$ and $\hat{N}$ being the number of particles value and operator respectively. This construction used by Levy-Lieb, allows to extend the set of densities to N-representable explicitly known sets instead of using v-representation. The energy ground state can be defined as a functional of the external potential and a function of the particle number N

$$E[v,N] = \inf_{\hat{\rho}} \{ tr(\hat{\rho}\hat{H}) \, | \, tr(\hat{\rho}\hat{N}) = N \} \quad . \tag{2.17}$$

Since for a given potential v, the ground state existence is not guaranteed for every particle number N, the infimum replaces the minimum in the expression 2.17.

Lieb's Convex Analysis

Despite that the basic DFT theorem guarantees a mapping one to one (at most) from a density to a potential, there is not necessarily an unique density for a given potential. If the functional is convex, any local minimum is also the global minimum. To assure this feature, Lieb constructed an universal density functional as the Legendre transform of $E[v]$ using convex analysis. The ground state energy $E[v,N]$ is a convex function of N for fixed v and a concave functional of v for fixed N

$$E[cv_1 + (1-c)v_2, N] \geq cE[v_1, N] + (1-c)E[v_2, N] \tag{2.18}$$

$$E[v, cN_1 + (1-c)N_2] \leq cE[v, N_1] + (1-c)E[v, N_2], \quad 0 \leq c \leq 1 \tag{2.19}$$

Using the convexity of $E[v,N]$ in N with the gauge property, a new functional G can be defined as the Legendre transform of the ground state energy with the pair of transformations

$$E[v,N] := \sup_{\mu} \{ N\mu - G[v,\mu] \} \tag{2.20}$$

$$G[v,\mu] := \sup_{N} \{ \mu N - E[v,N] \} = -\inf_{N} \{ E[v-\mu, N] \} \stackrel{def}{=} G[v-\mu] \tag{2.21}$$

Since $G[v-\mu]$ (which has only one functional dependence) is convex in v, it can be back and forth Legendre transformed [7]. This property is useful to define a functional Legendre transformation H of G with $-n$ as dual variable of v

$$\tilde{H}[-n] = \sup_{v} \{ -(n|v) - G[v] \} \stackrel{def}{=} H[n] \tag{2.22}$$

$$G[v] = \sup_{n} \{ (v|-n) - \tilde{H}[-n] \} = -\inf_{n} \{ H[n] + (v|n) \} \tag{2.23}$$

Inserting (2.23) in (2.20) it is obtained

$$E[v,N] = \underset{\mu}{sup}\{N\mu + \underset{n}{inf}\{H[n] + (v|n)\}\} \tag{2.24}$$

$$= \underset{\mu}{sup}\{\underset{n}{inf}\{\mu(N-(1|n)) + H[n] + (v|n)\}\} \tag{2.25}$$

$$\leq \underset{n}{inf}\{\underset{\mu}{sup}\{\mu(N-(1|n)) + H[n] + (v|n)\}\} \tag{2.26}$$

$$\leq \underset{n}{inf}\{H[n] + (v|n) + \underset{\mu}{sup}\{\mu(N-(1|n))\}\} \tag{2.27}$$

The last supremum can be either $+\infty$, if $(1|n) \neq N$, or zero, if $(1|n) = N$. Taking the infimum over all n implies the last case, and then the Variational Principle by Hohenberg and Kohn it's obtained in a satisfying logical context

$$E[v,N] = \underset{n}{inf}\{H[n] + (v|n) \mid (1|n) = N\} \tag{2.28}$$

Solving this functional leads to determination of the ground-state density and system's energy but its analytical form is unknown. A guess of the density functional $H[n]$ seems equally hopeless as a direct guess of $E[v]$.

Kohn-Sham equation

The development that made DFT a success was proposed by Sham and Kohn. It consisted in the subtraction from the Hohenberg-Kohn density functional of the Hartree energy ($E_H[n]$) and the ground state kinetic energy for an interaction free N-particle system with same density distribution as the interacting system ($T_0[n]$). A new functional

$$E_{XC}[n] = F_{HK}[n] - T_0[n] - E_H[n] \quad , \tag{2.29}$$

designated exchange-correlation energy functional is defined, where $T_0[n]$ and $E_H[n]$ are respectively given by

$$T[n] = \underset{\phi_i^*,\phi_i}{min}\{-\frac{1}{2}\sum_{i=1}^{N}\langle\phi_i|\nabla^2|\phi_i\rangle \mid \langle\phi_i|\phi_j\rangle = \delta_{ij},\ \sum_{i=1}^{N}\phi_i\phi_i^* = n\} \tag{2.30}$$

$$E_H[n] = \frac{1}{2}\int d^3r\, d^3r'\, n(\vec{r'})w(|\vec{r}_i - \vec{r}_j|)n(\vec{r}) \tag{2.31}$$

This trick simplifies the Hohenberg-Kohn functional treatment and allows to define the kinetic energy functional by setting all the unknown/complex interactions in $E_{XC}[n]$ which is much smaller than $F_{HK}[n]$ [6]. From(2.14) and (2.29), a ground state functional is obtained by minimising in ϕ_i^*

$$\frac{\partial E[n]}{\partial \phi_i^*} = 0 \tag{2.32}$$

$$= -\frac{\nabla^2}{2}\phi_i + \frac{\partial E_H}{\partial n}\frac{\partial n}{\partial \phi_i^*} + \frac{\partial E_{xc}}{\partial n}\frac{\partial n}{\partial \phi_i^*} - \varepsilon_i\phi_i \tag{2.33}$$

$$= (-\frac{\nabla^2}{2} + V_H(\vec{r}) + V_{xc}(\vec{r}))\phi_i - \varepsilon_i\phi_i \tag{2.34}$$

The introduced Lagrange multipliers ε_i guarantee the fulfilment of the physical conditions of (2.30). The equation obtained

$$(-\frac{\nabla^2}{2} + V_H(\vec{r}) + V_{xc}(\vec{r}))\phi_i = \varepsilon_i\phi_i \tag{2.35}$$

is known as the Kohn-Sham equation, and the respective non-linear operator as the Kohn-Sham operator, which depends on ϕ_i. The problem has to be solved self-consistently. The exchange-correlation potential expression is unknown and represents one of the biggest challenges to DFT, although there are good approximations developed from the Local Density Approximation (LDA) namely the Generalized Gradient Approximation (GGA) and the Local Spin Density Approximation (LSDA) which have a good accuracy.

LDA+U

The general idea of LDA is to take the known result for a homogeneous system and apply it locally to a non-homogeneous system

$$E_{xc}[n] \approx E_{xc}^{LDA} = (\varepsilon_{xc}(n(\vec{r}))|n(\vec{r})) \quad , \tag{2.36}$$

where $\varepsilon_{xc}(n(\vec{r})$ is the exchange-correlation energy of a homogeneous electron gas with same density distribution as the non-homogeneous system. Defined E_{xc}, the exchange correlation potential is given by

$$V_{xc} := \frac{\partial E_{xc}[n]}{\partial n(\vec{r})} = \varepsilon_{xc}(n(\vec{r}) + n(\vec{r})\frac{\partial \varepsilon_{xc}(n(\vec{r}))}{\partial n(\vec{r})} \quad . \tag{2.37}$$

Although the simplicity of this approximation, the LDA exchange-correlation functional leads to relatively convincing results [6].

Some d and most of f transition metals present strongly correlated electrons which cannot be successfully described in standard DFT methods. The LDA plus interaction term U (LDA+U) approach is an "on top of LDA" modification which allows to treat strongly correlated materials. For the localized d and f states, the Coulomb interaction of the electrons is formulated so a repulsion term U describing an intra atomic Hubbard interaction is included. This term tends to drive correlated orbital occupation numbers (n_i) to integer values 0 or 1 [8]. In a simple version of LDA+U method the shift on the LDA eigenvalues is [6]:

$$\varepsilon_i = e_i^{LDA} + U(\frac{1}{2} - n_i) \tag{2.38}$$

that is, more than half filled bands are shifted down in energy, while less than half filled bands are shifted up.

The addition of a Hubbard U interaction also introduces the need of "double counting" correction terms in the energy functional since the Coulomb energy was already included in the functional. Then the LDA+U method depends on the choice of the double-counting term.

2.2 Computational Details

2.2.1 Full-potential local-orbital

Between DFT solvers it is possible to distinguish the use of different potentials, different treatments of the atomic core states and different basis set for the Kohn-Sham operator. The choice of the basis set is an important issue in a DFT solver, in the way that one as to juggle between the accuracy of the numerical method and the numerical effort. The Full-potential local-orbital (FPLO) code [9] is highly accurate and numerically very efficient [10], due to the basis set construction technique - linear combination of local orbitals (LCLO).

This basis scheme is based on the Linear Combination of Atomic Orbitals (LCAO) method and adds one attractive potential to the atomic Kohn-Sham potential to solve the problem of incompleteness of

the LCAO basis [10]. The potential used to calculate the basis states is the sum of an atomic or ionic potential added with the potential

$$V_{LCLO} = \left(\frac{r}{\alpha_0 \, r_{max}} \right)^{n_0} + \Theta(r_{max} - r) \quad , \tag{2.39}$$

in which $\Theta(x)$ behaves like an infinite barrier potential to $r > r_{max}$. The parameters α_0 and r_{max}, reduce the variational freedom and completeness of the basis, but simplify the calculations. Nevertheless, the completeness can be recovered afterwards with the introduction of additional states. A much more detailed description about the FPLO code can be found on [9].

2.2.2 Force Theorem

Since magnetocrystalline anisotropy arises from spin orbit coupling, it is necessary to perform full relativistic calculations. The full relativistic calculations are very expensive numerically, difficulty that can be overcome in systems where spin-orbit interaction effects are small by:

- Treating the spin-orbit interaction as a perturbation with respect to other effects reducing the problem of calculating the difference in total energy for two directions of magnetization to the calculus of the difference between two sums of single-particle eigenvalues;
- Starting from a converged density matrix of a self-consistent spin-polarized scalar-relativistic calculation and solving the Kohn-Sham equations non self-consistently with the spin-orbit perturbation term included obtaining a slightly different total energy, energy eigenvalues and density matrix. The change obtained in the total energy is given in first order by the change in the energy sum over occupied single-particle states [11]. This relation has been called force theorem;

The evaluation of the MAE using the Force Theorem, which requires much less numerical effort, can be done by the following steps:

1. A scalar relativistic spin-polarized calculation is first converged;
2. The magnetization direction $< hkl >$ is specified and the eigenvalue problem with a converged potential is solved in a single step full relativistic calculation;
3. The sum of eigenvalues E_{hkl} up to the Fermi energy (the Band Energy) is evaluated for different $< hkl >$ and used to determine the anisotropy;

For systems with cubic symmetry only three calculations with magnetization along $< 001 >$, $< 111 >$ and $< 110 >$ directions are necessary to determine the first and second anisotropy constants [12]

$$K_1 = 4(E_{110} - E_{001}) \quad , \tag{2.40}$$

$$K_2 = 9(3E_{111} + E_{001} - 4E_{110}) \quad . \tag{2.41}$$

2.2.3 Parameters

The DFT code used for the simulations was the FPLO (version *14.00-47-x86-64*), and as convergence criteria for the simulations the standard accuracy value was chosen for both Density and Energy (1×10^{-6} a_0^{-3} and 1×10^{-8} Ha). The exchange-correlation functional used in all simulations was GGA with the parametrization of [13]. This choice is justified by the interest to compare the obtained results with

similar computations [12] using the same potential, and by the better performance of GGA over LSDA for most of 3d transition metals on calculating the lattice constants and in most cases also the magnetic moments [6].

The DFT calculations were done for two different crystalline compounds: magnetite and maghemite. The crystalline structure of magnetite can be described (at room temperature) as an inverse spinel structure with cations Fe^{3+} occupying the tetrahedral sites (A) along with a mixture of Fe^{2+} and Fe^{3+} on octahedral sites (B) of a fcc structure defined by the oxygen anions. Magnetite possess a half metal to insulator transition known as Verwey transition (at $T = T_V$), characterized by a spontaneous ordering of octahedral ion cations [14]. The induced change of crystal symmetry (from cubic to monoclinic) changes the anisotropy energy. Instead of the cubic anisotropy expression, below T_V , the expression for the monoclinic case should be used [12]:

$$\varepsilon_{ani} = K_a m_a^2 + K_b m_b^2 - K_u m_{\bar{1}01}^2 + K_{aa} m_a^4 + K_{bb} m_b^4 + K_{ab} m_a^2 m_b^2 \quad . \tag{2.42}$$

The anisotropy of the cubic and monoclinic phases are related and K_1 for the monoclinic case can be approximated by an average value of the low temperature phase monoclinic anisotropy constants [15]

$$K_1 = \frac{1}{45}(-20K_{aa} - 20K_{bb} - 6K_{ab}) \quad . \tag{2.43}$$

This K_1 value for low temperatures agrees with a linear extrapolation of the cubic phase data ($T > 300K$) [15]. And so the anisotropy K_1 determined for the cubic symmetry magnetite can be used as a good approximation for the cubic anisotropy constant of the monoclinic system at low temperatures. The magnetite (Fe_3O_4) structure was described with the following configuration [16]:

- Space Group: 227 (Fd-3m);
- Lattice parameter: 8.3941$\dot{A}$
- Wickoff Positions (x,y,z):
  - Fe: $\frac{1}{8}$ $\frac{1}{8}$ $\frac{1}{8}$ (multiplicity 8, A-sites)
  - Fe: $\frac{1}{2}$ $\frac{1}{2}$ $\frac{1}{2}$ (multiplicity 16, B-sites)
  - O: 0.2549 0.2549 0.2549 (multiplicity 32)

This configuration defines a unit cell with 8 formula units of magnetite, However due to the symmetry relations there are only 14 independent atoms (2 fu). The application of an uniaxial strain along the z-direction on this structure, reduces the system symmetry from fcc to bct lattice [17]. The space group of this structure belongs to a group which is a maximal subgroup of the space group 223. Using the program WYCKSPLIT [18], the Wyckoff positions on the tetragonal structure were obtained:

- Space Group:141 ($I4_1/amd$)
- Lattice parameter: a = 5.93553 $\dot{A}$, c = 8.3941 $\dot{A}$
- Wyckoff Positions (x,y,z):
  - Fe: 0 $\frac{3}{4}$ $\frac{1}{8}$ (multiplicity 4)
  - Fe: 0 0 $\frac{1}{2}$ (multiplicity 8)
  - O: 0 0.0098 0.2549 (multiplicity 16)

As can be seen by the multiplicities, the unit cell of this structure contains only half of the default configuration atoms but maintains the number of independent atoms.

Maghemite ($\gamma - Fe_2O_3$) can be described structurally as magnetite with iron deficiency. This is done setting the occupancy of the iron atom in the B-site to 5/6 [19], however the FPLO does not support currently a Wyckoff position with fractional occupancy. It is necessary then to use a tetragonal supercell structure $1 \times 1 \times 3$. While in the former configuration the vacancy distribution can be considered totally random, on the later it is generally admitted that the vacancies are ordered. Based on the structure used by [19], the maghemite configuration chosen was:

- Space Group: 96 ($P4_32_12$)
- Lattice parameter: a = 8.33 $\dot{A}$, c = 3a
- Wyckoff Positions (x,y,z)[2]:
  - Fe: $\frac{4}{8}$ $\frac{6}{8}$ $\frac{1}{24}$ (multiplicity 8)
  - Fe: 0 $\frac{2}{8}$ $\frac{1}{24}$ (multiplicity 8)
  - Fe: $\frac{2}{8}$ $\frac{4}{8}$ $\frac{3}{24}$ (multiplicity 8)
  - Fe: $\frac{5}{8}$ $\frac{3}{8}$ $\frac{2}{24}$ (multiplicity 8)
  - Fe: $\frac{1}{8}$ $\frac{5}{8}$ 0 (multiplicity 8)
  - Fe: $\frac{3}{8}$ $\frac{1}{8}$ $\frac{2}{24}$ (multiplicity 8)
  - Fe: $\frac{1}{8}$ $\frac{7}{8}$ $\frac{2}{24}$ (multiplicity 8)
  - Fe: $\frac{3}{8}$ $\frac{3}{8}$ 0 (multiplicity 4)
  - Fe: $\frac{7}{8}$ $\frac{7}{8}$ 0 (multiplicity 4)
  - O: $\frac{1}{8}$ $\frac{1}{8}$ $\frac{2}{24}$ (multiplicity 8)
  - O: $\frac{5}{8}$ $\frac{5}{8}$ $\frac{2}{24}$ (multiplicity 8)
  - O: $\frac{5}{8}$ $\frac{3}{8}$ 0 (multiplicity 8)
  - O: $\frac{3}{8}$ $\frac{1}{8}$ 0 (multiplicity 8)
  - O: $\frac{5}{8}$ $\frac{7}{8}$ 0 (multiplicity 8)
  - O: $\frac{1}{8}$ $\frac{7}{8}$ 0 (multiplicity 8)
  - O: $\frac{5}{8}$ $\frac{1}{8}$ $\frac{2}{24}$ (multiplicity 8)
  - O: $\frac{3}{8}$ $\frac{3}{8}$ $\frac{2}{24}$ (multiplicity 8)
  - O: $\frac{3}{8}$ $\frac{7}{8}$ $\frac{2}{24}$ (multiplicity 8)
  - O: $\frac{7}{8}$ $\frac{3}{8}$ $\frac{2}{24}$ (multiplicity 8)
  - O: $\frac{7}{8}$ $\frac{7}{8}$ $\frac{2}{24}$ (multiplicity 8)
  - O: $\frac{1}{8}$ $\frac{5}{8}$ $\frac{2}{24}$ (multiplicity 8)

With this configuration, the unit cell has 32 units of Fe_2O_3, and 160 independent atoms (which implies a heavy calculation for DFT).

An intermediary structure with an iron/oxygen ratio between magnetite and maghemite was also constructed. For it, all atomic positions of the magnetite (56) were determined within $P1$ symmetry and randomly one iron atom from an octahedral site was removed. In order to perceive the sensitivity of this choice, 5 different configurations were used but none of the corresponding calculations converged (with 7 subdivisions of Brillouin Zone) in order to relax the structure. A different iteration mode was also tried, with a reduced mixing between the new determined density and the density result in the previous iteration step, but without better results. Consequently, it was not possible to study this intermediate structure.

After a first set of trial simulations, it was proven necessary, to set the initial spin polarization of the Fe(A) and Fe(B) atoms with opposite sign in order to guarantee convergence of the system to the magnetic state of minimal energy - a ferrimagnetic state.

[2]The first three iron atoms in the following list are in tetrahedral sites while the others are in octahedral sites.

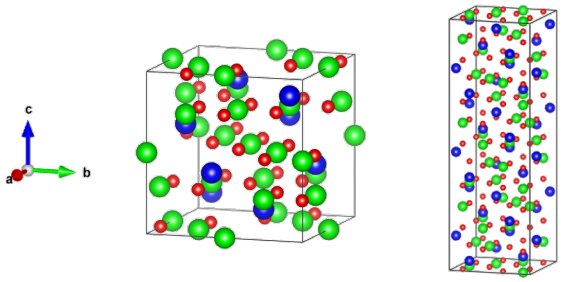

Figure 2.1: Crystalline structures used for Fe_3O_4 (fcc) , at left, and for Fe_2O_3, at right. The red balls denote oxygen atoms, the blue balls denote A-site (tetrahedral) iron atoms, and the green balls denote B-site (octahedral) iron atoms.

2.3 Simulations

2.3.1 K-Points Convergence

To compute the density of states and the charge density as well as other physical properties, it is necessary to integrate functions over the first Brillouin Zone (BZ). Due to the crystal inherent symmetries, the integration can be confined into a smaller region of the k-space designated irreducible wedge of the Brillouin zone, saving numerical effort. The integration is performed numerically by a weighted sum over the k-point mesh.

It is of major importance to test the computed parameters convergence with the number of k-points, in order to assure the result's stability. This is also important for computational optimization, since the more k-points are included, the bigger is the numerical effort and necessary resources. It is then essential to understand how to minimize the number of k-points used without compromising the result's accuracy. In the input file of *FPLO* a vector of 3 integers is specified which defines the BZ's subdivision along 3 axis from which the k-space integration mesh is constructed.

Since the BZ depends mostly of the crystalline structure, it is reasonable to assume that small variations on the used parameters do not require a new k-point convergence test, unless these variations induce a change on the system symmetry.

In Figure 2.2 the anisotropy constants convergence for the magnetite structure in a GGA+U calculation is shown, indicating that 10795 k-points (corresponding to the division of a Brillouin zone 33,33,33) is sufficient for the convergence of K_1 and K_2. For the *bct* magnetite structure in Figure 2.9, 11403 k-points (BZ division 32,32,32) allow for the anisotropy constants convergence.

The results for the convergence test of K_1 are shown in Figure 2.4 for maghemite. Unfortunately convergence can not be assumed, a small variation on the scale presented is too big to considerer a convergence scenario. The necessity of using a structure with so many independent atoms (160), makes the calculations numerically heavy and it was not viable to increase the number of BZ subdivisions taking in account the required time and computational resources.

2.3.2 LDA+U

The LDA+U method was used with the Atomic Limit functional with orthogonal projection of the states [12][20], method known to improve the description of correlated electrons. To compare the FPLO performance with previous results [12] and to determine the impact of this method on the results, the potential was varied for $U_{eff} = 0, 2, 4.5$ and 7 eV (with a division of the Brillouin zone 33,33,33) as single parameter.

To illustrate the effects of using the Hubbard Potential to describe the 3d iron electrons, the density

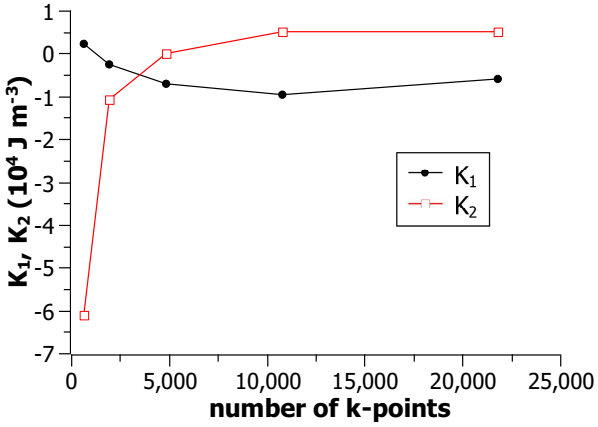

Figure 2.2: Calculated cubic anisotropy constants for the stoichiometric Fe_3O_4 as functions of the number of k-points in the irreducible wedge of the Brillouin zone with $U_{eff} = 4.5\ eV$.

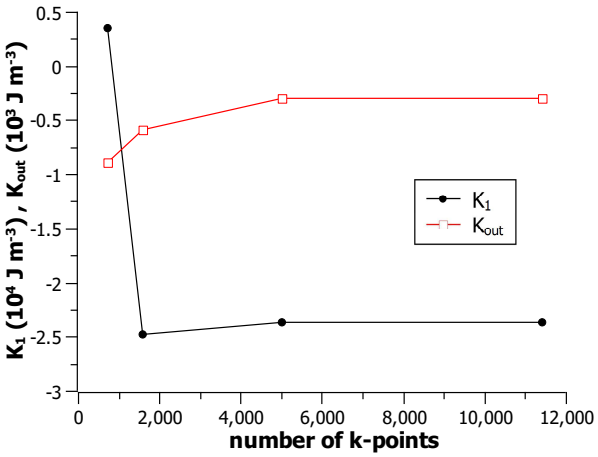

Figure 2.3: Calculated anisotropy constants for the tetragonal Fe_3O_4 as functions of the k-points number in the irreducible wedge of the Brillouin zone.

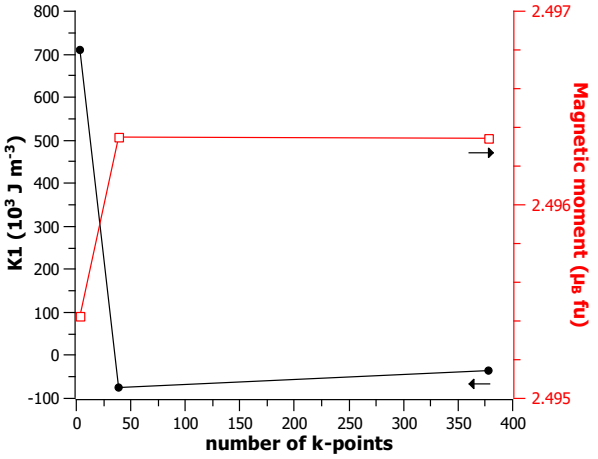

Figure 2.4: Calculated first cubic anisotropy constant (black) and magnetic moment (red) for the Fe_2O_3 as functions of the k-points number in the irreducible wedge of the Brillouin zone.

of states (DOS) for a GGA+U calculation ($U_{eff} = 4.5$) and for a GGA calculation ($U_{eff} = 0$) is shown in Figure 2.5. The comparison indicates a clear increase of the gap between the valence states (3d) and the core states, suggesting that the formers became more localized with the use of GGA+U, which is a better description of the real scenario.

In Figure 2.6 the anisotropy constants computed for the different U_{eff} are plotted, K_2 does not change much, but K_1 seems to converge for $U_{eff} \geq 4.5$ approaching zero, while for $U_{eff} \to 0$ its value increases in absolute value as other reported results [12]. It is important to highlight that the MAE for a cubic system is very small being difficult to calculate and frequently sensible to the calculation scheme used. This makes the disagreement of results between methods and DFT codes very difficult to identify and classify. The pointed difficulties associated with the calculus are such that a good agreement between the experimental K_1, and especially K_2, with the calculated ones could be a fortuitous coincidence.

The values computed for K_1 are close to the values reported in similar calculations by [12], while the values for K_2 do not have even the same sign. This difference is not unexpected due the referred difficulties associated with MAE calculations. Nevertheless, in both set of results the direction of easy magnetization is $< 111 >$ (Table 2.1). The reported value estimated by extrapolation for K_1 is $-2.7 \times 10^4\ J/m^3$ [17] closer to the result obtained for $U_{eff} = 0\ eV$, than the one obtained for $U_{eff} = 4.5\ eV$.

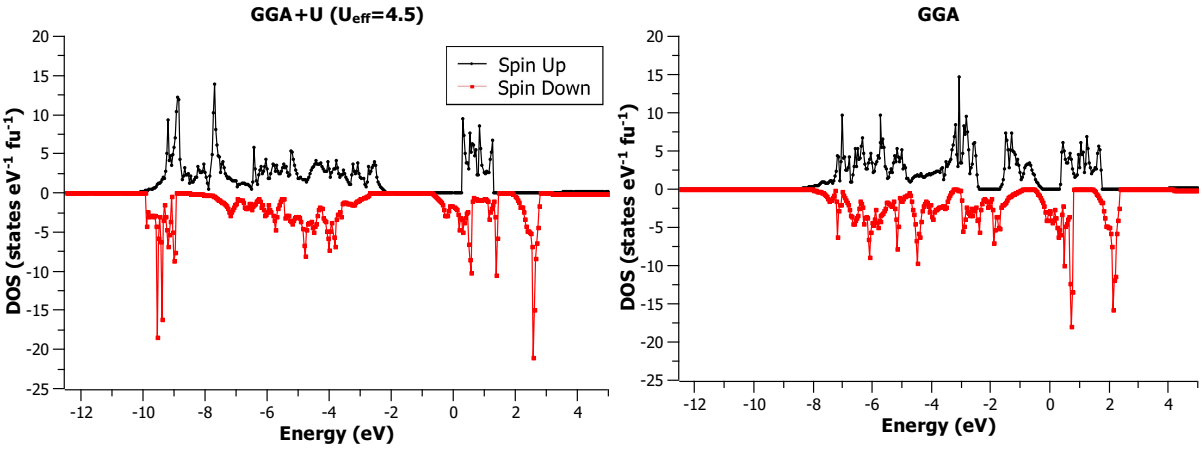

Figure 2.5: Computed scalar-relativistic DOS with (left) and without (right) Hubbard term for the stoichiometric Fe_3O_4 (with BZ division 32,32,32). The Fermi level is at zero energy.

The apparent tendency to reduce the absolute value of K_1, already difficult enough to determine in cubic systems, suggests that the introduction of the Hubbard Potential does not favour the calculations.

As seen in Figure 2.7 the total magnetic moment does not vary much with the effective potential used and seems to converge for $U_{eff} \geq 4.5$. Accidentally, it was discovered that for GGA+U calculations using the default configurations for the initial spin polarization ($2.00\mu_B$ for every atom) a metastable ferromagnetic state for magnetite is reached. Considering the magnetic exchange interaction as an Ising-type like interaction, the exchange constant (J) can be determined. Since the energy difference of the two magnetic configurations is equal to twice the exchange energy, attending to equation 2.7, J is given by

$$J = \frac{E_{ferrimagnetic} - E_{ferromagnetic}}{4NS_1S_2} \quad , \tag{2.44}$$

where N is the number of interacting pairs. In the magnetite crystalline structure two independent A-site iron each one having 12 B-site iron neighbours, 24 pairs, were considered. The calculated J for different U_{eff} are plotted in the Figure 2.7. The results are of the same order of magnitude of the value $3.87 \times 10^{-22}\ J/m^3$ estimated using a molecular field approximation [21] and considering a magnetite's Curie temperature of 854 K [14]. It is important to note that in some cases J is defined as twice the value used here [4], and there is the possibility that the values obtained in the molecular field approximation uses this definition. Multiplying by two the value of J obtained for $U_{eff} = 4.5$ the value $3.03 \times 10^{-22}\ J/m^3$ is obtained, very close to the reported estimation. The fact that this effective potential was successfully used to explain the contact hyperfine field in a number of iron oxides [12] supports the assumption that it is a good choice for the calculations on magnetite, and that the difference between the exchange constants is due to the different definitions of J.

2.3.3 Strain Effects

The DOS calculated using both bct and fcc unit cells for magnetite are compared in the Figure 2.8. As can be seen, they are nearly identical, confirming the correct construction of the magnetite crystalline structure using the tetragonal description. To obtain structures with lateral strain in the $< 001 >$ plane of 3.0%, 1.4%, 0.6%, 0.2% and the corresponding negative values, the lattice parameters were varied keeping the unit cell's volume constant. The lateral lattice strain is defined by

$$\xi = \frac{a}{a_0} - 1 \quad , \tag{2.45}$$

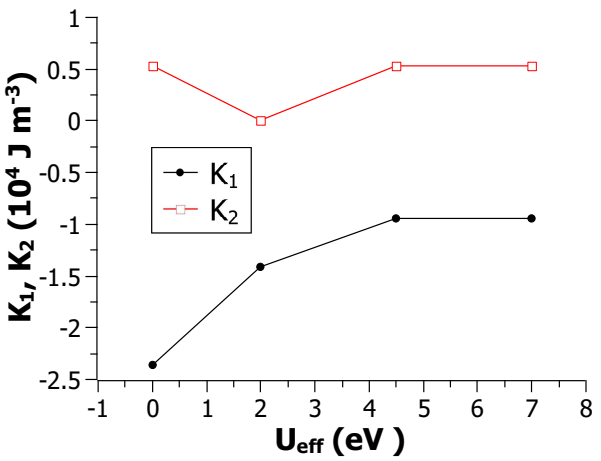

Figure 2.6: Variation of the cubic anisotropy constants for the stoichiometric Fe_3O_4 (with BZ division 33,33,33) as functions of the parameter U_{eff}.

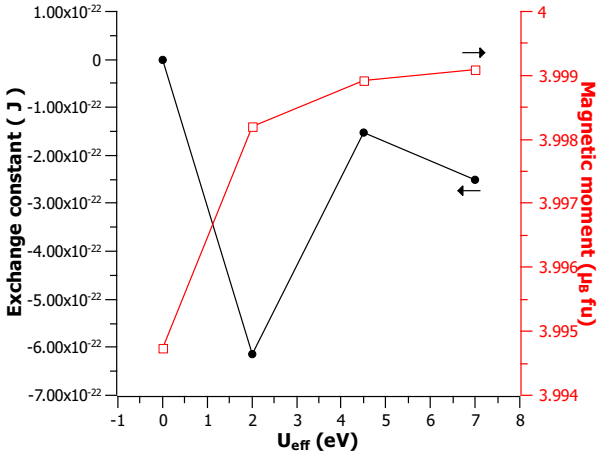

Figure 2.7: Variation of the exchange constant (black) and the magnetic moment (red) for the stoichiometric Fe_3O_4, along the $< 001 >$ direction (with BZ division 33,33,33) as functions of the parameter U_{eff}.

Table 2.2: Lattice constants used to induce strain on the bct magnetite.

Strain (%)	a (Å)	c (Å)	V ($Å^3$)
-3.0	5.757	8.921	295.728
-1.4	5.852	8.634	295.728
-0.6	5.900	8.496	295.728
-0.2	5.924	8.428	295.728
0.2	5.947	8.361	295.728
0.6	5.971	8.294	295.728
1.4	6.019	8.164	295.728
3.0	6.114	7.912	295.728

where a_0 is the unstrained lattice parameter. The lattice parameters values for this study are presented in Table 2.2. Taking in account that the transformation from a fcc to a bcc is done with a $\frac{\pi}{4}$ rotation on the plane $< 001 >$, the cubic $< 110 >$ and $< 100 >$ directions are interchanged on the tetragonal lattice. To be comparable with the cubic case, K_1 is in this case obtained by

$$K_1 = 4(E_{100} - E_{110}) \quad . \tag{2.46}$$

In Figure 2.9 the K_1 results for the different applied strains are plotted. This parameter does not change its value for small strains ($< 1\%$) and displays different behaviour for higher tensile/compressive strains as reported for similar calculations [17]. An increase in the K_1 absolute value for more tensile (negative lateral strain) strains is obtained while under application of higher compressive strain (positive lateral strain), K_1 approaches zero. The results for the anisotropy out of strain plan (K_{out}) are plotted in Figure 2.9, obtained by

$$K_{out} = E_{110} - E_{001} \quad . \tag{2.47}$$

A monotonous increase of K_{out} with applied strain is obtained. This monotonous behaviour implies a preference of the magnetization to lie along the compressed direction. This property can be used to induce perpendicular magnetization on thin films since the shape anisotropy energy should be nearly independent of the strain [17] and $|K_{out}| > |K_1|$.

The calculated K_1 values are close to the reported in similar calculations [17] while the K_{out} values

are smaller in magnitude, but in both the same relative behaviour is obtained. The existing difference is not unexpected since a different exchange potential (LSDA) was used in the reported simulations [17].

In Figure 2.10 the magnetic moment variation of A-site and B-site iron ions with strain is shown. The total magnitude does not change considerably due to the similar variation on both sites and anti-symmetric orientation of the two magnetic moments of the ions. In the total magnetic moment these variations compensate.

To compute the exchange constant a calculation GGA+U with $U_{eff} = 4.5\ eV$ was performed but did not converge. An intermediate computation was done for $U_{eff} = 0.5\ eV$ and the obtained density used as initial in the $U_{eff} = 4.5\ eV$ case.

In Figure 2.11 the exchange constants computed for the different strains are plotted. As in the previous set of simulations, a ferromagnetic metastable state was obtained using GGA+U (with initial spin polarization of both iron atoms set as $2.0\mu_B$) with $U_{eff} = 4.5$. The result for the non-strained bct structure is equal to the obtained previously in the fcc case, which is a good sign of consistency. Although, the strain induces a considerable variation on the exchange constant, with a symmetric response (almost) for compressive (positive lateral strain) and tensile (negative lateral strain) stress. An analysis of the energy variation as function of the applied strain for both magnetic phases reveals little sensitivity of the ferromagnetic phase to the considered lattice parameters changes. The behaviour observed in Figure 2.11 is similar to the energy variation obtained for the ferrimagnetic case, with the cubic structure not being the energy minimum. This result (obtained for $T = 0K$) is in agreement with the expected magnetite crystalline structure (monoclinic) below the temperature of Verwey.

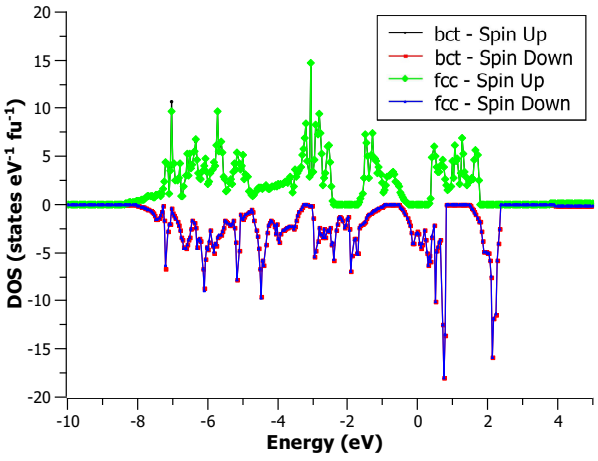

Figure 2.8: Comparison of the scalar-relativistic DOS between the stoichiometric and tetragonal Fe_3O_4 (with BZ division 32,32,32). The Fermi level is at zero energy.

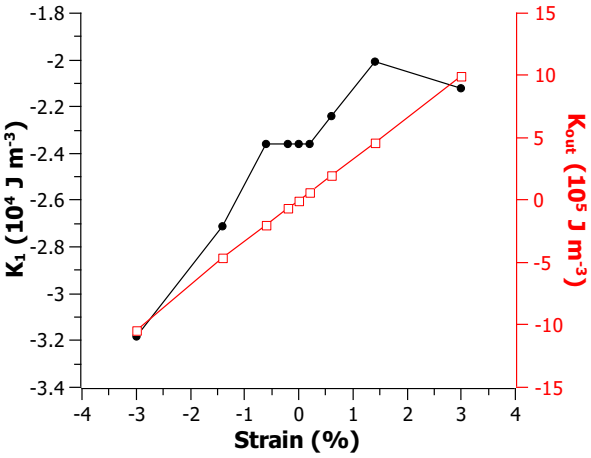

Figure 2.9: Variation of the anisotropy constants for the tetragonal Fe_3O_4 (with BZ division 32,32,32) as functions of the lateral strain.

2.3.4 Iron deficiency

As already referred the anisotropy constant K_1 did not converge for the maghemite. Nevertheless it is possible to retrieve some information from the DOS (Figure 2.12) and the magnetic moment. In the Figure 2.4 it is plotted the computed net magnetic moment which seems to have converged with the magnetic moment of the ions $3.82\mu_B$ (B-sites) and $3.35\mu_B$ (A-sites, absolute value). The exchange constant J is related via mean-field theory with the Curie temperature [21]

$$T_C = 4\frac{J_{AB}}{k_B}\sqrt{2S_AS_B(S_A+1)(S_B+1)} \quad . \tag{2.48}$$

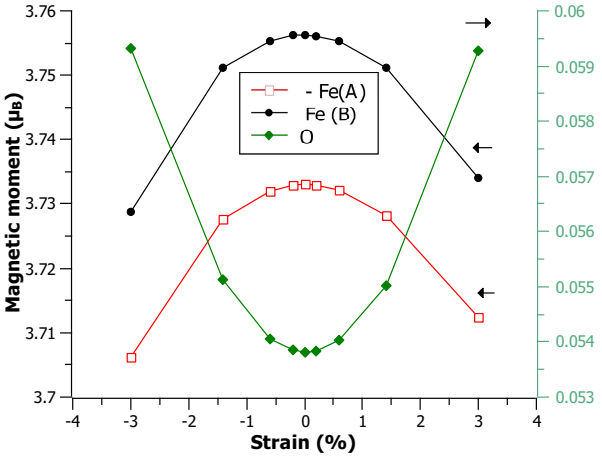

Figure 2.10: Variation of the atomic magnetic moment for the tetragonal Fe_3O_4 (with BZ division 32,32,32) as function of the lateral strain.

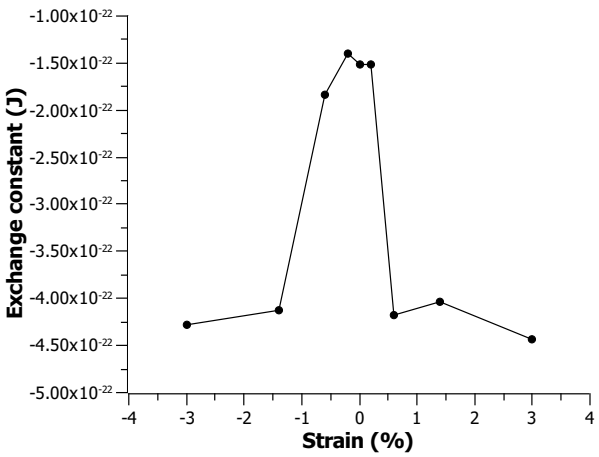

Figure 2.11: Variation of the exchange constant for the tetragonal Fe_3O_4 (with BZ division 32,32,32) as function of the lateral strain.

Since the mean-field theory tends to overestimate the Curie temperature, corrections are added for the different crystal structures. For a fcc structure, such as magnetite and maghemite, a closer estimate is given by [21]

$$T_C' = 0.789 T_C \left(1 - \frac{0.13}{\sqrt{S_A S_B (S_A+1)(S_B+1)}} \right). \tag{2.49}$$

Using 919.15 K as T_C' [14], a value of 5.83×10^{-22} J was estimated for the exchange constant assuming a g-factor of 2.00 and the ion spin (S) calculated from the magnetic moment as $\mu = g\mu_B S$ (orbital magnetic moment is quenched).

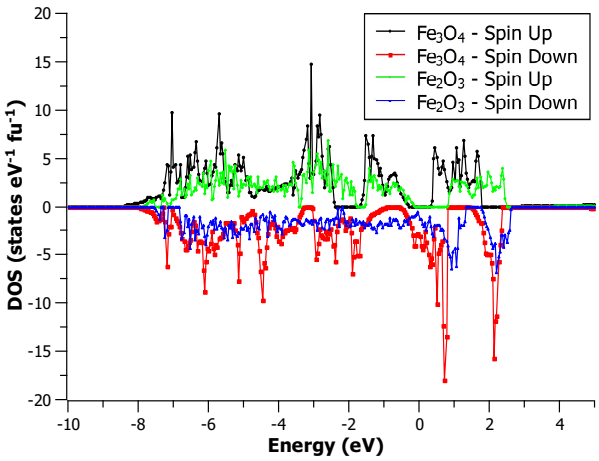

Figure 2.12: Comparison of the scalar-relativistic DOS between the stoichiometric Fe_3O_4 (with BZ division 32,32,32) and Fe_2O_3 (with BZ division 7,7,7). The Fermi level is at zero energy.

2.4 Discussion

Both compounds, magnetite and maghemite, show a (scalar-relativistic) DOS characteristic of a half-metal (Figure 2.12), with a half filled band for one spin orientation, and an insulator or semiconductor band like for opposite spin orientation. With this band structure an integer magnetic moment is predicted result that is another characteristic of stoichiometric half metallic compounds since within the insulator/semiconductor spin channel an integer set of bands are fully occupied and each one holds one down

electron per unit cell. Also the number of electrons occupying the unit cell of stoichiometric compounds is integer, implying that the conductor spin channel must also have an integer number of bands fully occupied. For scalar-relativistic calculations, this property has been verified for the unit cell of magnetite with magnetic moment $8.00\mu_B$ and the cell used for maghemite with $80.00\mu_B$. When the spin-orbit coupling (included in fully relativistic calculations) is taken in account, it induces a small orbital moment. However this induced moment is small for 3d electrons, and magnetic moments near integer values are still expected. The values obtained per unit cell for the magnetite and maghemite were 7.998 and 79.883 bohr magnetons respectively.

The use of LDA+U as method to improve the magnetic description of stoichiometric Fe_3O_4, was found to be unnecessary. No significative gain was obtained on the net magnetic moment calculation, which was already close to the expected value, and on the anisotropy constants (Figure 2.6). As U_{eff} increases, it is observed a divergence from the reported estimated value [17] as the K_1 computed values approach zero. This tendency may add difficulties on the cubic anisotropy constant value computation. Nevertheless, it allows to do an approximation of J by letting the system converge to a ferromagnetic metastable state, for reasons which are not clear but may be related to the better description of 3d electrons (observed in the DOS, Figure 2.5). For $U_{eff} = 4.5$ the obtained J is closer to the mean-field estimation (half of its value), being no surprise since it was also the best potential for the description of hyperfine fields in oxides [12]. Taking all this in consideration, the required extra numerical effort for doing a LDA+U calculation is justified to determine J.

By comparison with the references [12] and [17] on the MAE's results, the FPLO method consistently underestimated the anisotropy constants in absolute value. Yet, it described well the general behaviour and sign of K_1. The differences must be related with the DFT code itself, since the method LDA+U used (functional and double-counting scheme) is the same as [12]. Another source of deviation for the MAE's results may be the use of the force theorem approximation, which may not be appropriate for these systems. An attempt was made, to perform a self-consistent full relativistic calculation to compare with the obtained results for the stoichiometric magnetite, but convergence was not obtained in the simulations for all the required magnetization directions. The slow increase of U_{eff} from a converged density till 4.5 eV or the slow rotation of the magnetization direction from one converged solution in to the desired direction did not solve the convergence problem.

Comparing the parameters calculated for the fcc and bct (without strain) structure is observed coherency within the obtained results. The computed magnetic moments, K_1, and J (computed with $U_{eff} = 4.5\ eV$) are essentially equal for both structures.

In Figure 2.13 the relative variation of the parameters studied with uniaxial strain is shown (mediated by the bct values). The net magnetic moment can be considered approximately constant. The anisotropy constant K_1 remains of the same the order of magnitude although for bigger strains ($|\xi| \geq 1.4\%$) some variation is observed specially in compressive strains. The K_1 negative values imply that for all the considered strains magnetization orients along $< 110 >$ or $< 111 >$ (depending on the value of K_2, (Table 2.1) rather than $< 001 >$. In the cubic limit this means that there is no alteration of the easy and hard directions of magnetization. In this sense the cubic anisotropy constant K_1 may be considered independent of the applied strains.

In contrast with the referred parameters, the calculated exchange constant J changes abruptly by more than 100% for strains (-0.6% $\geq \xi \geq$ 0.2%). The increase of J (absolute value) implies a bigger critical size for single domain magnetic nanoparticle, not compromising the physical properties, only in $\xi = -0.2\%$ there is a small decrease of the exchange constant not significant. It is hard to understand if the behaviour obtained for J is adequate or not, since an Ising like interaction may not describe correctly

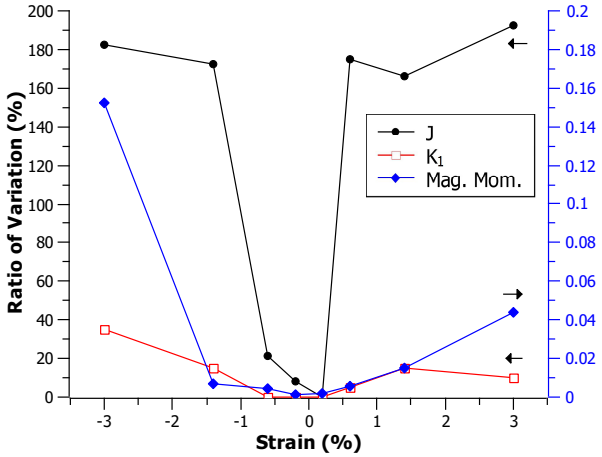

Figure 2.13: Ratio of variation of the magnetic moment (blue), the exchange constant (black) and the first cubic anisotropy constant (red) for the tetragonal Fe_3O_4, relatively to the values obtained in the unstrained (tetragonal) structure.

the phenomena associated (exchange mediated by O atoms), even if the values calculated for the *bct* (no strain) and fcc structures are close to the expectations. Also, the variation obtained is affected by the use of a cubic/tetragonal symmetry that does not correspond to the system structure at $T = 0K$.

For ferrimagnetic materials the net magnetic moment depends on the unequal contribution of the two magnetic sub-lattices, in both magnetite and maghemite this inequality results from the two different position of iron ions Fe(A) and Fe(B). Since in maghemite the proportion $A : B$, 3:5, is smaller than the 1:2 of magnetite, it is expected a smaller net magnetic moment. The value obtained in the simulations per unit formula was $3.999\mu_B$ and $2.496\mu_B$ for magnetite and maghemite respectively, which is in accordance with the expectation. The experimental values of the Curie temperatures indicate that $J_{Fe_2O_3} > J_{Fe_3O_4}$ as obtained [14]. Unfortunately it was not possible to obtain convergence for K_1 in maghemite to verify if the iron deficiency would induce any variation on the directions of easy and hard magnetization.

Chapter 3

Micromagnetic Calculations

3.1 Introduction

3.1.1 Magnetic Concepts II

Magnetization

The magnetization ($\vec{M}$) is a measure of the magnetic state of the system, it expresses the density of net magnetic dipole moments $\vec{\mu}$ in the material being a very useful quantity for treating magnetic systems within the continuous approximation.

$$\vec{\mu}_{Total} = \int \vec{M}(\vec{r})\, dV \tag{3.1}$$

In vacuum there is no magnetization, and the magnetic field can be identically described by the vectors $\vec{H}$ and $\vec{B}$ which differ only by a multiplicative constant (ε_0). In general, the relation between these magnetic field vectors is more complicated and they may be very different in magnitude and direction. Generically the relation between $\vec{H}$ and $\vec{B}$ involves $\vec{M}$ and is given by

$$\vec{B} = \mu_0(\vec{H} + \vec{M}) \quad , \tag{3.2}$$

in a magnetic system. The magnetic polarization ($\vec{J}$) which is linearly related with the magnetization is frequently used in the numerical treatment of these systems

$$\vec{J} = \mu_0 \vec{M} \quad . \tag{3.3}$$

Zeeman Energy

Classically, in the absence of a magnetic field the energy of an isolated magnetic dipole does not depend on its orientation. When a magnetic field $\vec{B}$ is applied, this symmetry is broken, and the energy dependence on the magnetic moment orientation is given by the Zeeman Energy

$$E_Z = -\int \vec{M}.\vec{B}\, dV \quad . \tag{3.4}$$

The lowest energy state corresponds to the magnetic moment being aligned with the applied field.

Magnetostatic Energy

The magnetostatic energy, also known as demagnetization energy, arises from the classical dipolar interaction between the magnetic moments, and in a continuous model, can be written as the interaction of the magnetic moment $\vec{M}dV$ of the volume element dV with the magnetic moment of the remaining volume. This interaction generally favours the reduction of the total magnetic moment, via formation of magnetic domains. It depends strongly on the geometry of the system, being also designated shape anisotropy, and can induce a preferred direction of magnetization.

For a ferromagnetic material, assuming a continuous material and using the Maxwell's equations in absence of currents

$$\nabla \times \vec{H} = 0 \quad , \tag{3.5}$$

$$\nabla . \vec{B} = 0 \quad . \tag{3.6}$$

The first equation states that $\vec{H}$ is irrotational so it can be written as the gradient of a scalar field [5]

$$\vec{H} = -\nabla U \quad . \tag{3.7}$$

Using this definition on Maxwell's second equation and taking in account of the relation between $\vec{H}$, $\vec{B}$ and $\vec{M}$, the potential inside the body obeys

$$\nabla^2 \vec{U} = \nabla . \vec{M} \quad . \tag{3.8}$$

and outside the body, $\vec{M} = 0$ obeys

$$\nabla^2 \vec{U}_{out} = 0 \quad . \tag{3.9}$$

At the surface both potentials are expected to follow the boundary conditions

$$\vec{H}_{out\parallel} - \vec{H}_{in\parallel} = \vec{J}_s = 0 \quad , \tag{3.10}$$

$$\vec{B}_{out\perp} - \vec{B}_{in\perp} = 0 \quad . \tag{3.11}$$

The first condition imposes continuity of the potential U at the surface $\vec{U}_{out} = \vec{U}_{in}$, while the later implies

$$\frac{\partial \vec{U}_{out}}{\partial \vec{n}} - \frac{\partial \vec{U}_{in}}{\partial \vec{n}} = \vec{n} . \vec{M} \quad , \tag{3.12}$$

where $\vec{n}$ is the unit normal to the body's surface. Also U is required to be regular at infinity [5]. Once U is determined, the demagnetization field H_{demag} can be calculated (Equation 3.7), and the demagnetization energy can be evaluated as

$$E_{demag} = -\frac{\mu_0}{2} \int \vec{H}_{demag} . \vec{M} \, dV \quad , \tag{3.13}$$

where a factor $\frac{1}{2}$ is introduced to avoid double counting the interaction of A with B, and B with A [5].

There are very few cases where it is possible to determine U analytically but if the body is uniformly magnetized the demagnetization field is proportional to magnetization

$$\vec{H}_{demag} = -D\vec{M} \quad , \tag{3.14}$$

where D is the demagnetization tensor, for the trivial case of a spherical sample this tensor is diagonal and equal to $\frac{1}{3}$. For a prolate or an oblate ellipsoid, with the axes $a = b$, the demagnetization factors can be calculated respectively as [22]

$$D_z = \frac{1}{\alpha^2 - 1} \left(\frac{\alpha}{2\sqrt{\alpha^2 - 1}} \ln \left(\frac{\alpha + \sqrt{\alpha^2 - 1}}{\alpha - \sqrt{\alpha^2 - 1}} \right) - 1 \right), \quad \alpha = \frac{c}{a} \quad , \tag{3.15}$$

$$D_z = \frac{\beta^2}{\beta^2 - 1}\left(1 - \frac{1}{\sqrt{\beta^2 - 1}}\arcsin\left(\frac{\sqrt{\beta^2 - 1}}{\beta}\right)\right), \quad \beta = \frac{a}{c} \quad , \tag{3.16}$$

with the other components of D given by

$$D_x = D_y = \frac{1 - D_z}{2} \quad . \tag{3.17}$$

The demagnetization tensor components depend only on the ratio between the ellipsoid axes and not on their absolute values. For an elongated shape the demagnetization field favours a magnetization along the major axis.

The numerical evaluation of this energy is one of the most challenging parts in micromagnetic calculations since dipolar interactions are long-ranged.

3.1.2 Micromagnetism Theory

The Micromagnetism theory is an approach to explain the magnetization reversal and hysteresis effects (between other processes) in ferromagnetic materials at an intermediate length scale between magnetic domains and crystal lattice sites. At this scale, due the dominance of exchange interactions, the magnetization should not change direction abruptly and can be described by a continuous function. This approach allows the calculation of magnetization structures, the determination of magnetization reversal and the derivation of relevant expressions considering the exchange energy important contribution and calculating the Zeeman, Magnetostatic and Anisotropy interactions as perturbation terms [23]. The referred interactions do not modify the magnetization magnitude, but change its direction acting as torques on the magnetic moments, $\vec{M}dV$, of the volume elements dV. At equilibrium, $\vec{M}$ is oriented such that the total torque on each volume element is zero [24].

To use an energy method instead the calculation of torques, it is necessary to define an expression for the energy. The magnetization configuration must guarantee both external and internal equilibrium implying the use of a Gibbs free energy [24], that should include the appropriate energy contributions (which may depend of the system) and is written in the continuous approximation

$$E = \int \left(\varepsilon_{ani} + \varepsilon_{demag} + \varepsilon_Z + \varepsilon_{exch}\right) dV \quad . \tag{3.18}$$

Due to its natural discrete description the exchange energy distinguishes itself from the other terms, requiring an approximation by a continuous function. With that purpose equation (2.7) is recalled and written in terms of the angle $\phi_{i,j}$ between spin i and spin j as

$$E_{exch} = JS^2 \sum_{neighbors} \phi_{i,j}^2 \quad , \tag{3.19}$$

since the angles between neighbouring spins are expected to be small. The magnetization's versor ($\vec{m}$) should be locally parallel to the spin moments allowing to approximate $\phi_{i,j} \approx |\vec{m}_i - \vec{m}_j|$, and since $\vec{m}$ is continuous, $|\vec{m}_i - \vec{m}_j|$ can expanded to first-order as

$$|\vec{m}_i - \vec{m}_j| = |\vec{r}_{ij}\nabla\vec{m}| \quad , \tag{3.20}$$

where $\vec{r}_i$ is the position vector from lattice point i to the neighbour point j. The exchange energy can then be written as

$$E_{exch} = JS^2 \int \sum_j |\vec{r}_j \nabla\vec{m}|^2 \, dV \quad . \tag{3.21}$$

For a cubic crystal the sum over j is a summation over the lattice primitive vectors and for all three cubic lattice types the integration differs only on a multiplicative factor [5]. A continuous expression for the exchange energy is then derived as

$$E_{exch} = A \int |(\nabla m_x)|^2 + |(\nabla m_y)|^2 + |(\nabla m_z)|^2 \, dV \quad , \tag{3.22}$$

where $A = n\frac{2JS^2}{a}$ is the structure stiffness constant with $n = 1, 2, 4$ respectively for a *sc*, *bcc* and *fcc* lattice [5] [24].

In thermodynamic equilibrium the system occupies a minimum energy state (not necessarily the global minimum) and the aim of Micromagnetics is to find the equilibrium magnetization configuration. Brown proposed a variational method based on the calculation of the variational derivative of the total energy with respect to the magnetization. To determine the minimum energy the coefficients of the linear term vanish for any variation $\delta\vec{m}$

$$\frac{\delta E}{\delta \vec{m}} = 0 \quad , \tag{3.23}$$

and the condition

$$\frac{\delta^2 E}{\delta \vec{m}^2} > 0 \quad , \tag{3.24}$$

guarantees the solution's stability.

Another important concept in Micromagnetics is the definition of effective magnetic field as the quantity obtained by differentiation of the free energy density:

$$E = -\int \vec{M}.\vec{B_{eff}} \, dV \quad , \tag{3.25}$$

$$\delta E = \int \frac{\delta \varepsilon}{\delta \vec{M}} \delta \vec{M} \, dV = 0 \quad \text{(equilibrium condition)}, \tag{3.26}$$

$$\Rightarrow \vec{B}_{eff} = -\frac{\delta \varepsilon}{\delta \vec{M}} \quad . \tag{3.27}$$

3.1.3 Landau-Lifshitz-Gilbert Equation

Although the minimization of the system free energy can be used to find an equilibrium magnetization distribution, the energy landscape of micromagnetic systems with many local maxima, minima, and saddle points can make minimization a very poor technique for predicting the correct minimum. A more realistic approach toward the system equilibrium position is provided by a dynamic description, due to the dynamic behaviour of many magnetic phenomena as for instance magnetization reversal. The Landau-Lifshitz-Gilbert (LLG) equation describes the precession with damping of the magnetic moment in a effective magnetic field and it is ideal for a dynamic approach of the magnetization evolution to equilibrium.

A free magnetic moment under an applied magnetic field experiences a torque which makes it precess - Larmor precession - around the local magnetic field, satisfying

$$\frac{\mathrm{d}\vec{M}}{\mathrm{d}t} = \gamma \vec{M} \times \vec{B} \quad . \tag{3.28}$$

If damping does not exist the magnetic moment can not relax to equilibrium. Since relaxation is observed experimentally and there are many magnetic phenomena which contribute to relaxation, it is necessary to add a term directed from $\vec{M}$ to $\vec{H}$ for the alignment to take place [25]

$$\frac{\mathrm{d}\vec{M}}{\mathrm{d}t} = \gamma \vec{M} \times \vec{B} + \alpha M_s (\vec{B} - \frac{(\vec{B}.\vec{M})}{M_s^2} \vec{M}) \quad . \tag{3.29}$$

Using the triple vector product, this equation can be rewritten in a more convenient form as

$$\frac{\mathrm{d}\vec{M}}{\mathrm{d}t} = \gamma\vec{M}\times\vec{B} - \frac{\alpha}{M_s}\vec{M}\times(\vec{M}\times\vec{B}) \quad , \tag{3.30}$$

which corresponds to the LLG equation where α is a dimensionless factor and γ is the gyromagnetic ratio. The equation remains valid for systems more complex than free magnetic moments. In magnetic domains, the other sources of torque, besides the external applied field are described by an effective magnetic field B_{eff}.

3.1.4 Finite Elements Method

The Finite Elements Method (FEM) is a numerical method to solve partial differential equations (PDE) that discretizes the continuum domain into smaller simple elements which collection is referred to as mesh or grid. Depending on the dimension of the problem the elements can be triangles, squares, or rectangles in two dimensions, or tetrahedrons, cubes, or hexahedra for three-dimensional problems [23]. This flexibility, useful to model complex geometries, makes FEM a powerful technique.

Essentially, the FEM is a minimization technique for variational problems. The solution of the PDE is approximated by piecewise continuous polynomials and the PDE is hereby discretized and split into a finite number of algebraic equations. Hence, the unknown coefficients of these polynomials are determined in a way that minimizes the distance to the exact solution. In simple terms, it is a procedure that minimizes the error of approximation by fitting trial functions into the PDE. Since the number of elements is finite, the problem of finding a continuous solution for the PDE is reduced to calculating the finite number of coefficients of the polynomials. These polynomials (u) are expanded at N nodal points of the mesh and interpolated in each element, using a basis functions set (φ_i)

$$u(\vec{r}) = \sum_{i=1}^{N} u_i\varphi_i(\vec{r}) \tag{3.31}$$

which have only local support

$$\varphi_i(\vec{r}_j) = \delta_{ij} = \begin{cases} 1, & i = j \\ 0, & i \neq j \end{cases} \quad , \tag{3.32}$$

($\vec{r}_j$ denotes the vector from the origin to the node j) [6]. Within the element the potential/functional $u(\vec{r})$ is the weighted average of its value at the nodal points that define the element.

Both static and dynamic micromagnetic FE calculations start from the discretization of the total magnetic Gibb's free energy. When $\vec{J}(r)$ is approximated by piecewise polynomial functions on the FE mesh, the energy functional reduces to an energy function with the nodal values of the polarization as unknowns. The construction of a suitable energy functional $I[\vec{J},\vec{A}]$ could be done with any expression whose minimum, obtained by differentiation with respect to potential vector $\vec{A}$ and being set equal to zero, is the field $\vec{J}(r)$ expression. This procedure performed for each nodal potential at each element in a set of linear algebraic equations which describe the entire region, allows to determine the distribution of $\vec{J}(r)$from the energy functional (rather than from the PDE) at the nodal points of the mesh and then suitably interpolate within each finite element [23].

Also, both static and dynamic micromagnetic calculations require evaluation of the effective field at the nodal points of the FE mesh, which is the sum of the exchange field, the anisotropy field, the magnetostatic field, and the external field. The latter, the exchange field and the anisotropy field depend only

locally on the magnetization or its spatial derivatives and thus may be directly calculated. The magnetostatic field requires a more complex treatment, since it is non local, depending on the magnetization distribution over the entire system, and an "open boundary" problem with one of its boundary conditions at infinity. There are different accurate and effective techniques well established for the FE calculation of magnetostatic fields.

3.2 Computational Details

3.2.1 MagPar

Between a wide variety of micromagnetic software packages available, the *MagPar*[26][27](version 0.9) was selected to perform the simulations. From another freely and widely used softwares like *OOMMF* and *Nmag*, the *MagPar* stands up for using a finite elements method instead of a finite differences method (as *OOMMF*), and for its performance. The method used by the software defines how the discretization of the spacial domain is typically done, for finite differences the three dimensional domain is subdivided in cubes while for finite elements is subdivided in tetrahedra (like in *MagPar*). The latter allows a more convenient approximation to geometries with curvature as the case of ellipsoidal nanoparticles.

Another advantage of the chosen micromagnetic package is the use of a hybrid finite element/boundary element method to compute the demagnetization field, which allows to avoid the numerically expensive evaluation via direct integration of Green's functions.

3.2.2 Parameters

As already discussed, magnetite and maghemite are ferrimagnetic materials. In order to study these materials within the micromagnetic approximation it is necessary to characterize the two ferromagnetic sub-lattices (A and B). Due to the exchange interaction between ions of the lattice A and B, the calculation of the respective effective fields [28] and the LLG equations are not independent. The referred iron oxides have an inverse spinel structure which have the property of negligibly small exchange energies (J_{AA} and J_{BB}) between ions in the same sub-lattice and then can be neglected comparing with the interaction between sub-lattices (J_{AB}) [21]. So it is not possible in this structures to decouple the sub-lattices and unfortunately the *MagPar* is not prepared to treat that coupling.

However since it can be considered only an exchange energy J_{AB}, the system has similarities to a ferromagnetic material. If a rescaling of the problem is done, and instead of consider the magnetic moments of the ions, the magnetic moment of the molecule (Fe_3O_4 or Fe_2O_3) is taken - a ferromagnetic system with J_{AB} of equal value but opposite sign is obtained as illustrated in Figure 3.1. At this scale it is plausible that the magnetization does not change abruptly and the micromagnetic theory be can applied without necessity of two different sub-lattices. The magnetite (Fe_3O_4) pa-

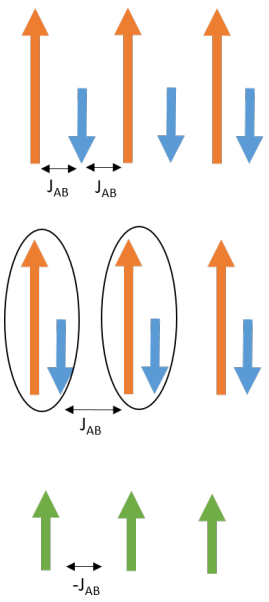

Figure 3.1: Scheme of a ferromagnetic approximation for a ferrimagnet.

rameters used on the micromagnetic simulations were: [1][2]

- $M_s : 501.406\, kAm^{-1}$;
- $A : 1.3233 \times 10^{-10}\, Jm^{-1}$;
- $K_1 : -1.1792 \times 10^{4}\, Jm^{-3}$;

and the maghemite (Fe_2O_3) parameters used were:

- $M_s : 427.049\, kAm^{-1}$;
- $A : 1.7219 \times 10^{-10}\, Jm^{-1}$, calculated using T_C as 919.15 K [14];
- $K_1 : -4.65 \times 10^{3}\, Jm^{-3}$ [14];

where K_1 is the magnetocrystalline anisotropy constant. Another parameter defined for the simulations was the dimensionless parameter α present in the LLG equation, which governs the rate of approach to equilibrium. For numerical convenience it is often set to a value between 0.1 and 1, which results in a reduced computation time [23]. A value of 0.1 was used in the studied cases for α, which should be the more appropriate for small nanoparticules. It is assumed that these parameters remain constant to all applied fields.

3.2.3 Discretization

The creation of a geometric model and respective discretization which defines the problem's mesh was done adopting the *Gmsh* (version 2.0.9) software as suggested on the *MagPar* manual. In micromagnetic calculations the domain discretization has to be done with the elements size smaller than the exchange length (the smaller feature of the system) in order to avoid abrupt changes of the magnetization as required by micromagnetic approximation. The exchange length considered should be the smaller of the two lengths (disregarding thermal effects) [29][26]:

$$l_{Néel} = \sqrt{\frac{2A}{\mu_0 M_s^2}} \quad , \tag{3.33}$$

$$l_{Bloch} = \sqrt{\frac{A}{K_1}} \quad . \tag{3.34}$$

For the compounds in the study, magnetite and maghemite, these lengths are $2.89 \times 10^{-8}\, m$ and $4.71 \times 10^{-8}\, m$ respectively, far bigger than the intended structures sizes.

Since *Gmsh* has two different algorithms (Tetgen+Delaunay or Netgen) for the three dimensional mesh generation a test for an uniformly magnetized prolate ellipsoid ($a = 5\ nm$ $c = 10\ nm$) was done in order to determine the most suitable choice. For the same initial mesh element size (l_0), a mesh was generated and had its quality optimized using each one of the algorithms. A smaller l_0 generates a mesh with bigger resolution and more elements, although the amount of them depends on the method used. The demagnetization energy of the system was then calculated using *MagPar*, with the magnetization aligned along the ellipsoid's major axis and the obtained value is compared with the theoretical value

[1] The values of A for both materials are miscalculated with a factor of 2, and the distance between Fe_A and Fe_B used as a. For magnetite, the critical size for a single domain particle obtained with the used value is very close to the expected [3].

[2] The K_1 value used for magnetite is miscalculated by a factor of 2, nevertheless, this does not alter the qualitative data obtained from the micromagnetic simulations.

plotting the relative difference on Figure 3.2. The comparison shows that the Netgen algorithm is more suitable since its demagnetization energy is closer to the expected theoretical value and has less mesh elements for the same l_0, implying less numerical effort.

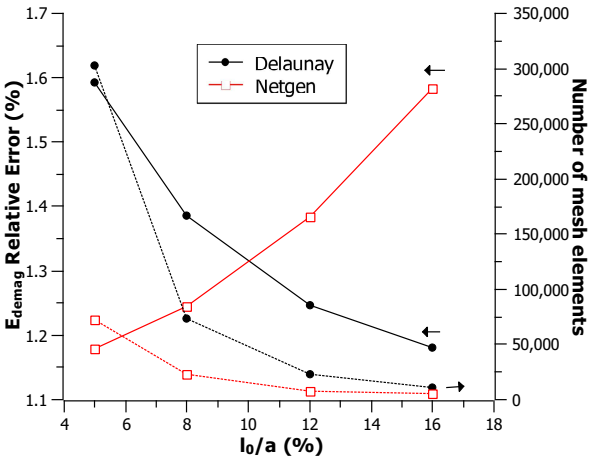

Figure 3.2: Comparison of mesh algorithms performance. The dotted lines corresponds to the number of elements generated with the respective algorithm and the solid lines correspond to the obtained demagnetization energy's relative error relatively to the theoretical value.

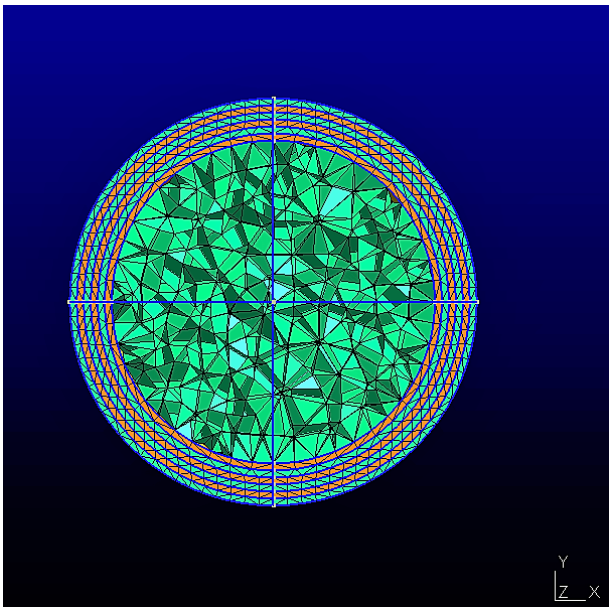

Figure 3.3: Cut on Z plane of the mesh generated for a calculation where the composition of the nanoparticle was changed.

The ellipsoid axis sizes used on the geometries and the corresponding volume computed by *MagPar* are shown in Table 3.1. The geometries volume is surprisingly around 6.7% smaller than the ellipsoid volume ($9202\,nm^3$). To investigate the source of this deviation, the volume of a sphere (with $r = 5\ nm$) generated with different l_0, was computed (Figure 3.4). The deviation was not sensible to the mesh resolution and cannot be then the source of deviation. Another possibility would be the discretization of the geometry curvature. To test this idea a sphere was generated with the two different commands available to draw curves on *Gmsh* (”Ellipse” and ”Circle”). As seen in Figure 3.4 the quality of the mesh generated using the geometry drawn with the ”Circle” command is far better and explains the observed deviation. Unfortunately the ellipsoid geometry can not use this alternative and, for consistency, to maintain the volume approximately constant, the spherical geometries were constructed with the ”Ellipse” command.

In order to study the effects of magnetite oxidation on the nanoparticles a shell composed of maghemite was implemented on the exterior of the geometry. This shell was subdivided in layers, as illustrated at Figure 3.3, to have a reasonable number of elements along radial direction without imposing a too fine mesh in the whole volume.

3.3 Simulations

3.3.1 Mesh Convergence

Studying the mesh convergence is crucial to guarantee accuracy in the results obtained, minimizing the numerical effort dispensed and ensuring that the mesh generated is appropriate for the problem. In a prolate ellipsoid the calculated demagnetization energy varies with the direction of magnetization as expected (Figure 3.5). The difference between the simulated values and the theoretical ones is not significant at the problem natural scale with the coarser mesh (with $l_0 = 1.0$) implying that there is no advantage in using finer ones.

Table 3.1: Geometric parameters of the studied ellipsoids of revolution, being the semi-principal axes of length a, b, c associated to the axis x,y,z respectively according the standard ellipsoid equation $\frac{x^2}{a^2}+\frac{y^2}{b^2}+\frac{z^2}{c^2}=1$. The parameter b was always defined with the same value as a.

c/a	a [nm]	c [nm]	V [nm^3]
2.00	10.3181	20.6362	8585.19
1.67	10.9573	18.2987	8586.04
1.44	11.5121	16.5775	8586.34
1.30	11.9114	15.4848	8586.75
1.20	12.2335	14.6802	8587.04
1.13	12.4810	14.1036	8586.84
1.09	12.6319	13.7687	8586.92
1.00	13.0000	13.0000	8586.99
0.90	13.4647	12.1182	8586.80
0.85	13.7237	11.6651	8587.07

Table 3.2: Geometric parameters for the studied layered spheres structures, being the d the depth of the outer shell and r the inner core radius.

f	d [nm]	r [nm]	V [nm]
1.00	1.5472	5.9528	1649.70
0.85	1.3905	6.1095	1650.30
0.75	1.2763	6.2237	1650.70
0.65	1.1530	6.3470	1651.10
0.50	0.9841	6.5519	1651.67

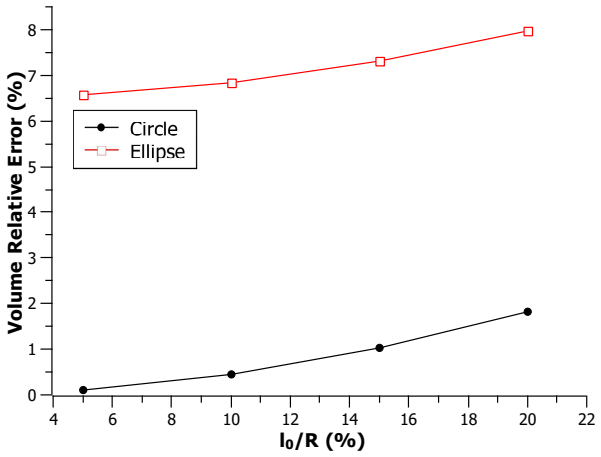

Figure 3.4: Comparison of the structure's volume relative error for meshes with curves generated either with the "Circle" or "Ellipse" commands as functions of the relative initial mesh length.

For the spherical structure with sub-layers in the outer shell, it is necessary to analyse how the number of layers used changes the computed values of E_{ani} and compare them to the theoretical estimate. This test is done for the anisotropy energy since a reasonable estimation for it can be done - a simple weighted mean, since both compounds share easy, medium and hard directions of magnetization (for the material's parameters used). Figure 3.6 (right) shows that the increase of sub-layers, reduces the deviation from the estimate. Since subdividing in 7 layers does not offer more accuracy than subdividing in 6 layers and that increasing the number of divisions can produce a more deformed mesh with less quality, it was found adequate to use 6 layers in the mesh. The deviation from the estimate value for this choice on the system's "natural scale" is plotted on the Figure 3.6 (left) showing the same behaviour and tendency in the limits $\frac{V_{Maghemite}}{V_{Magnetite}} \to 0$ and $\frac{V_{Maghemite}}{V_{Magnetite}} \to \infty$.

3.3.2 Geometry Variation

In single domain nanoparticles the exchange energy can be considered constant. As a result only the anisotropy (magnetocrystalline and/or shape) energy and the Zeeman energy must be considered to

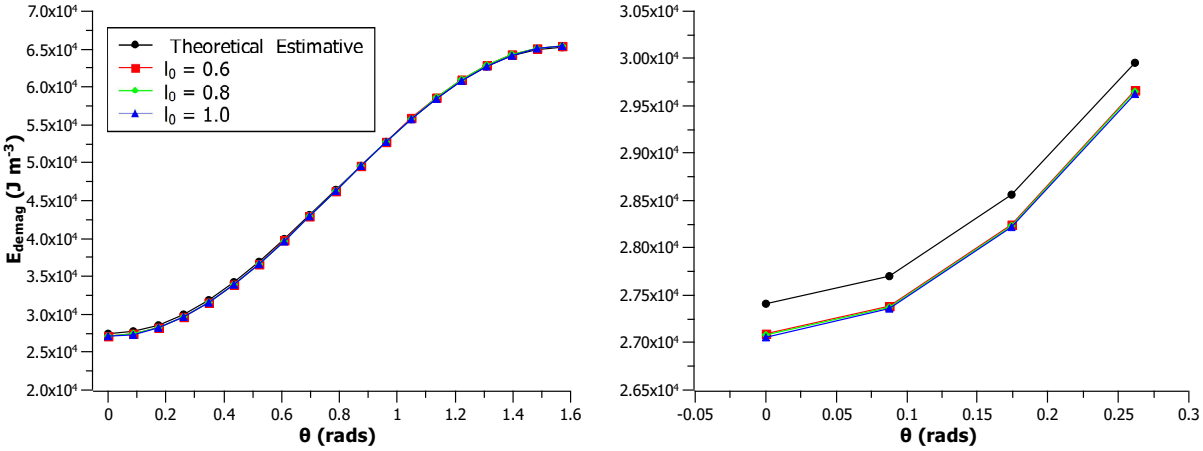

Figure 3.5: Variation of the demagnetization energy as function of the azimuthal angle theta for meshes generated with different initial mesh lengths and comparison with the theoretical estimate. At right is presented a zoom in of the region of small angles.

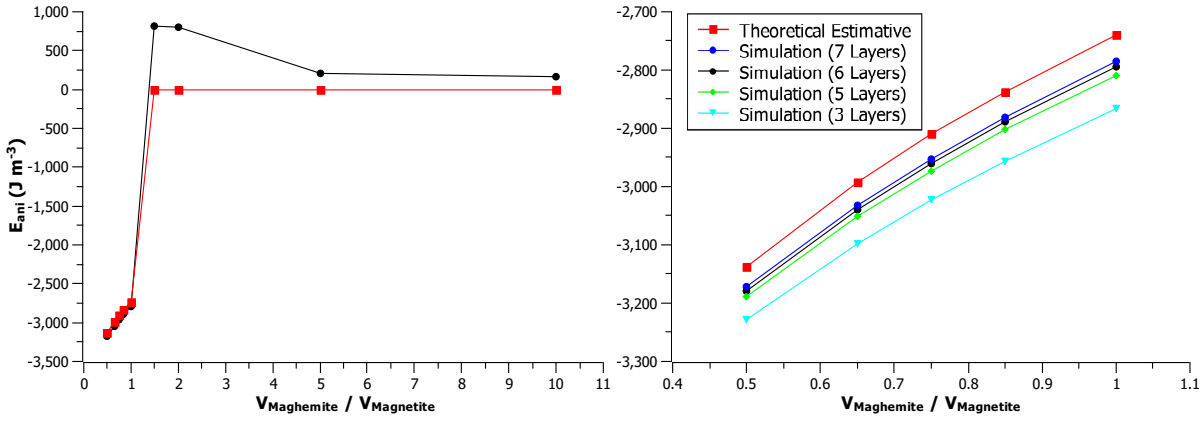

Figure 3.6: Variation of the anisotropy energy as function of the maghemite-magnetite volume fraction for structures with different sub-layers in the outer shell and comparison with the estimated values (right). Variation of the anisotropy energy at the problems natural scale for the used structure.

determine changes in the magnetization - this approach is known as the Stoner-Wohlfarth model. For uniformly magnetized ellipsoids of revolution the form of these energy terms are known and therefore the magnetization direction which minimizes the energy can be calculated as well the nucleation field defined as the field that cause instability in the magnetization direction.

In the sphere case ($c/a = 1$) the demagnetization field plays no role on setting the magnetization direction and it is the magnetocrystalline field that defines it. The direction of easy magnetization is $< 111 >$, translated as $\theta = \arctan[\sqrt{2}]$ (azimuthal angle) and $\phi = \frac{\pi}{4}$ (polar angle) on spherical coordinates. For $c/a > 1$ the demagnetization field will promote the alignment along z direction, while for $c/a < 1$ cases it promotes the alignment on the xy plane. Therefore the angle θ is the relevant variable and it is acceptable to fix the angle ϕ as $\pi/4$ in order to facilitate the theoretical calculation. Then the energy density for these ellipsoids in absence of a magnetic field is given by

$$\varepsilon(\theta, H) = K_1 \sin^2(\theta) \left[\frac{1}{4}\sin^2(\theta) + \cos^2(\theta)\right] + \frac{\mu_0 M_s^2}{2}\left[D_x \sin^2(\theta) + D_z \cos^2(\theta)\right] \quad . \tag{3.35}$$

Through minimization of this expression, the magnetization direction of equilibrium (θ_0) can be found. For the sphere ($c/a = 1$) the right term can be discarded since for this geometry the magnetostatic energy does not depend on the magnetization direction and is constant.

To evaluate the nucleation field it is necessary to consider the response to an applied magnetic filed (H), which can be done simply by adding in the expression above the Zeeman term

$$\mu_0 H M_s \cos(\theta - \theta_0) \quad . \tag{3.36}$$

Afterwards it is necessary to find the minimum absolute value of H for which the relaxed magnetization direction becomes unstable. Numerically this condition is satisfied for

$$\left|\frac{\partial E}{\partial \theta}\right| < tol \quad \text{and} \quad \frac{\partial^2 E}{\partial \theta^2} < tol \quad . \tag{3.37}$$

The parameter tol (tolerance) can be seen as the uncertainty associated with the zero value. The computations were effectuated in the *Mathematica* software (used code in Appendix) and the parameter tol was set to 10^{-4}.

The LLG relaxation allows to determine the magnetic configuration which minimizes the system energy and then determine which phenomena(s) rules on the magnetic particle. From an initial random magnetization, the LLG equation is solved until the convergence criteria is satisfied or the simulation time reaches t_{max}. The default convergence criteria on *MagPar* ($max\left|\frac{dM[element]}{dt}\right| < 10^{-5}$) was used for all simulations. Initially the LLG relaxation was done with $t_{max} = 3600\ ns$, which proved to be unnecessary large and 25 ns were considered sufficient. While most of the simulations satisfied the convergence criteria within the respective time ($t_{max} = 25\ ns$), for $\frac{c}{a} = 2.00$ and 1.00 this was not the case what does not imply necessarily non convergence. As can be seen on Figure 3.7 the magnetization can be already considered converged at 5 ns, but due to small deviations around the relaxed configuration the numerical convergence criteria is not satisfied.

In Figure 3.8 the obtained magnetization direction angles are plotted for the relaxed system as well as the expected theoretical values calculated via energy minimization. While the azimuthal angle (θ) obtained follows closely the expected tendency, the polar angle (ϕ) diverges from the expected constant value when the ratio $\frac{c}{a}$ increases. Since this divergence occurs for $\theta \to 0$, when the x and y components of magnetization go to zero, the ϕ contribution is irrelevant.

It is possible to distinguish within these results three different behaviours for the prolate ellipsoid: the demagnetization field completely defines the easy axis of magnetization (along z axis) making $\theta \to 0$ - for

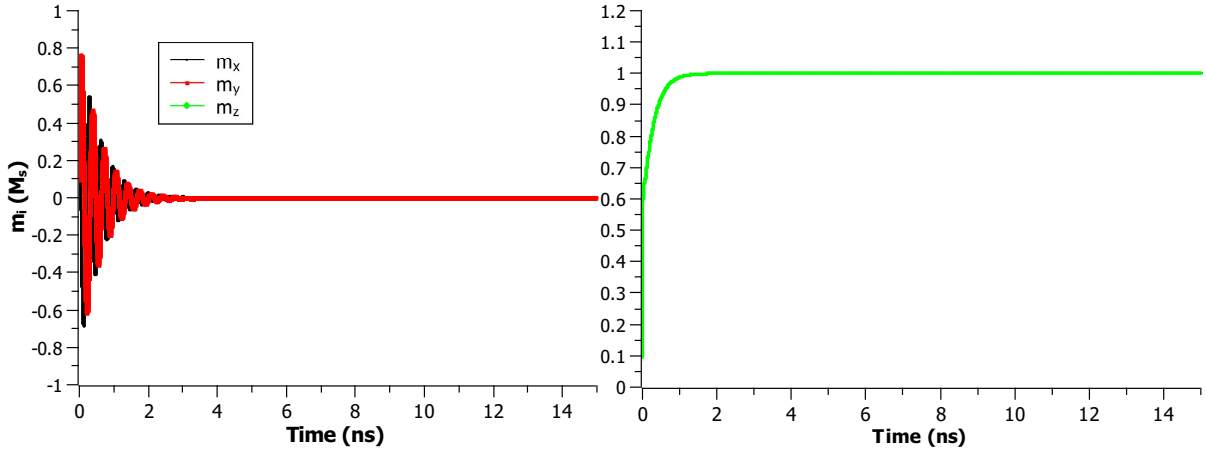

Figure 3.7: Variation of magnetization components as functions of time (left) for the ellipsoid with $c/a = 2.00$.

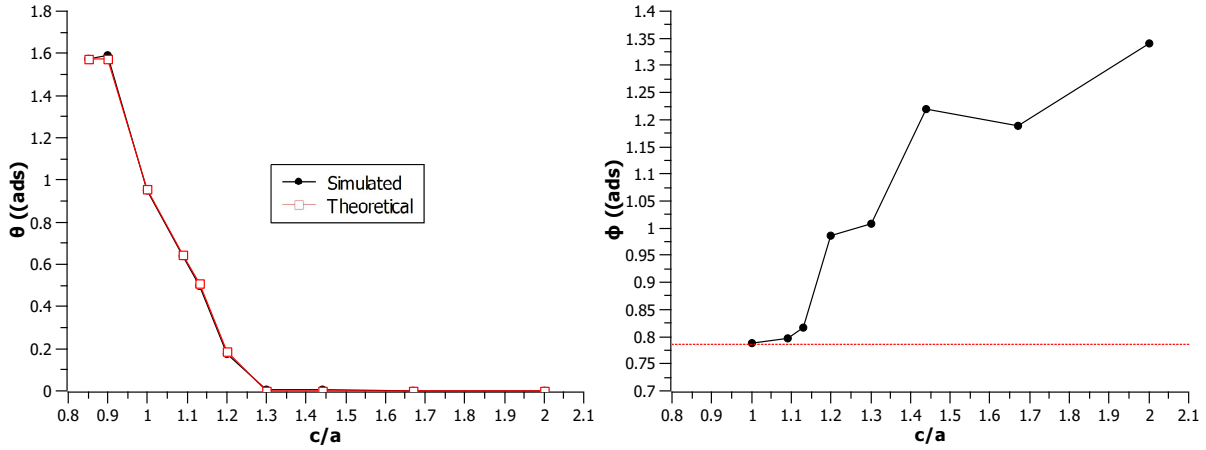

Figure 3.8: Variation of the magnetization's direction angles as function of the parameter c/a and comparison with estimated values (red). At left is presented the azimuthal angle (θ) and at right the polar angle (ϕ).

the ratios 2.00, 1.67, 1.44 and 1.30 ($\theta < 0.01$) - or the magnetocrystalline anisotropy field is comparable driving $\theta \to \arctan\left(\sqrt{2}\right)$ and $\phi \to \frac{\pi}{4}$ until it defines by itself the magnetization direction at $c/a = 1.00$ in the $< 111 >$ direction.

The hysteresis loop was obtained through application of a magnetic field in the same direction as the relaxed magnetization, the field's magnitude was then decreased in steps until it reached zero. Afterwards field's magnitude was inverted and increased until it reached the same absolute value as the initial one. For each field applied, the system was relaxed via LLG equation and the obtained magnetic configuration used as the initial one for the following step.

In Figures 3.9, 3.10, and 3.11 the obtained hysteresis loops are plotted which display the expected symmetry between the upward and downward curves. From these results the nucleation fields (H_n) were determined as the applied field (H_i) for which the magnetization is inverted, values that are plotted in Figure 3.12. To be more exact H_n can be any value in the interval $]H_{i-1}, H_i]$, what is translated into an uncertain of -1 kA/m taking in account the step used on the field variation. Besides the deviation between the values estimated theoretically and the ones computed through LLG, they share the same tendency. The deviation appears to increase as c/a approaches one, what may offer a hint of the deviation source since it is in this limit that the magnetocrystalline anisotropy becomes more significant. Also it should be remarked that ϕ was fixed on the theoretical estimation.

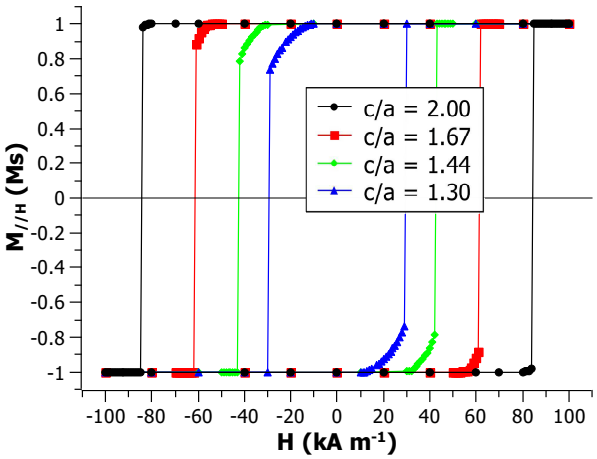

Figure 3.9: Hysteresis loops for prolate ellipsoids where the demagnetization energy defines the relaxed magnetization direction.

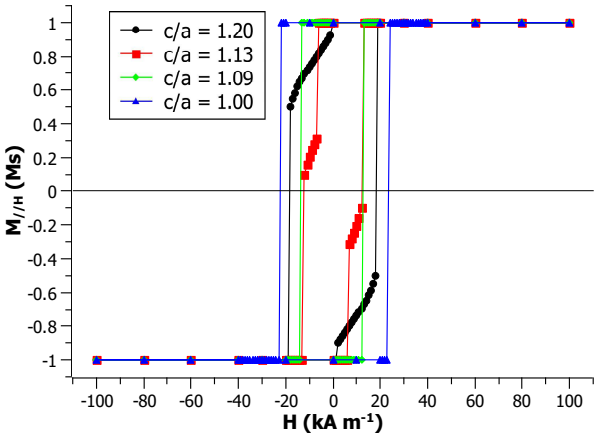

Figure 3.10: Hysteresis loops for prolate ellipsoids where the demagnetization energy competes with the magnetocrystalline energy.

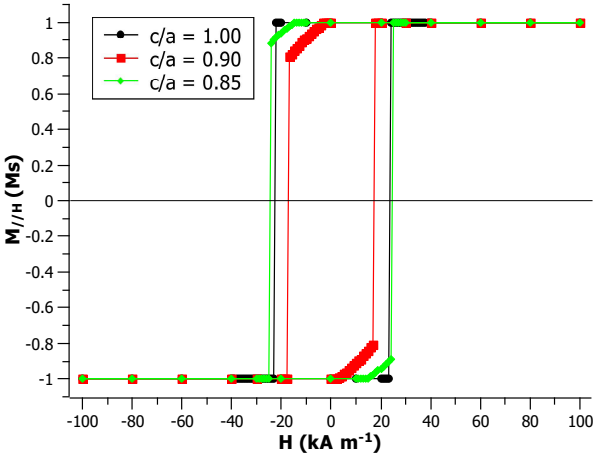

Figure 3.11: Hysteresis loops for the oblate ellipsoids studied.

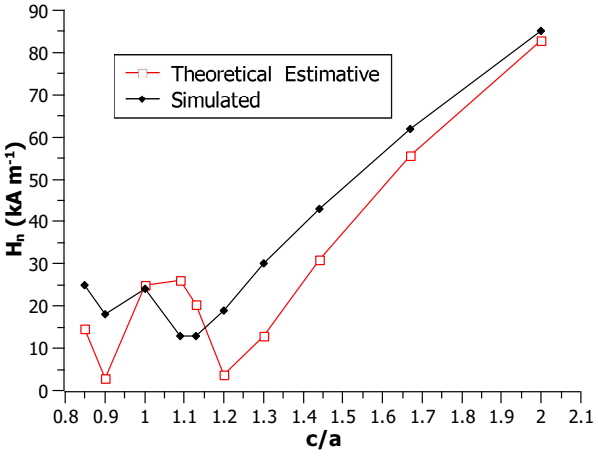

Figure 3.12: Variation of the nucleation field as function of the parameter c/a.

3.3.3 Composition Variation

Determining the nanoparticle's surface oxidization impact on the nucleation field requires a scenario of non uniform magnetization complicating the determination of the magnetostatic energy contribution. Yet it can be conjectured that for a sphere it does not depend on the magnetization direction, being the MAE the most relevant energy term for different magnetization orientations. The MAE term must be similar for magnetite and maghemite since they share the same directions of easy and hard magnetization. This energy term can be considered given by the weighted sum of the contributions from each compound in a composed particle. It is with this considerations in mind that the MAE was used for testing the mesh convergence.

The nucleation field can be estimated theoretically considering only the MAE contribution as [14]

$$H_n = \frac{4}{3}\frac{K_1}{\mu_0 M_s} \quad , \tag{3.38}$$

using K_1 and M_s as weighted sums: $\frac{V_{[Fe_3O_4]}}{V}X_{[Fe_3O_4]} + \frac{V_{[Fe_2O_3]}}{V}X_{[Fe_2O_3]}$.

From the experience obtained on the previous set of simulations, the relaxed magnetization direction determination through LLG relaxation was done with $t_{max} = 20ns$. The simulations did not fulfil the numeric convergence criteria within the time interval set, but post analysis of the magnetization showed that it had converged and the obtained magnetic configurations are aligned close to the expected direction (Figure 3.13). As can be seen in Figures 3.14 and 3.15 the magnetization discontinuity in the oxidized

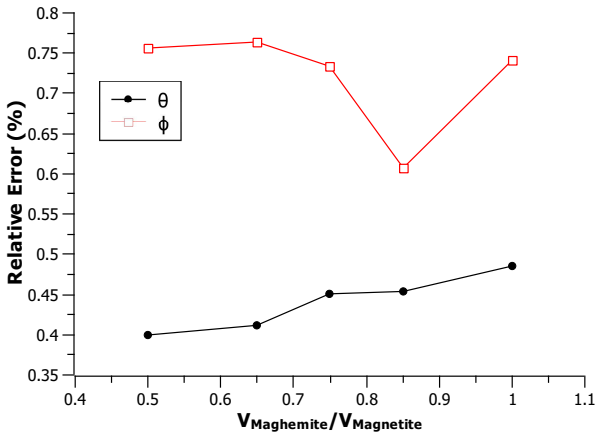

Figure 3.13: Relative error of the obtained magnetization's direction angles as function of the parameter f.

layer does not induce a visible change in the demagnetization energy and field. The energy estimated considering an uniform magnetized sphere is very close to the results obtained from the simulations and display the same tendency.

Since a different behaviour between the upward and downward curves is not expected in the hysteresis loop, and the *MagPar* performance has already been tested in this matter on the previous set of simulations, it is justified to compute only one curve. This is a convenient option due to the numerical effort required for this structures that is increased by the finer mesh at the shell. The obtained curves can be seen in Figure 3.16, and the nucleation fields calculated from them are plotted in Figure 3.17 with an associated uncertainty of $-0.5\ kA/m$ (taking in account the step used on the applied field variation).

Due to the difference between the compounds anisotropy constants, there was the possibility of having magnetization reversion on the shell under application of a magnetic field weaker than the core nucleation field which would show up as a step in the magnetization curve. This hypothesis is completely

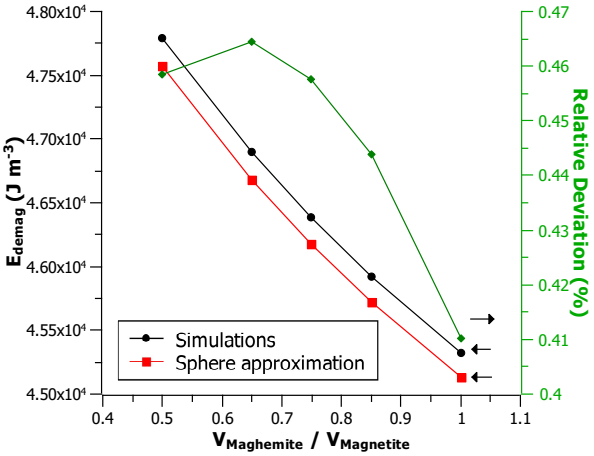

Figure 3.14: Variation of the demagnetization energy as function as the maghemite-magnetite fraction and comparison with theoretical estimate.

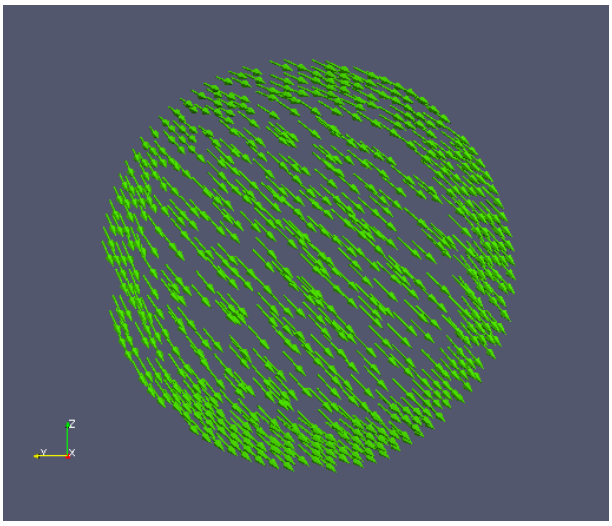

Figure 3.15: Representation of the demagnetization field obtained for the case with equal proportion of maghemite and magnetite.

discarded upon observation of the magnetization curves in Figure 3.16. An extra simulation for $f = 1.00$, without the demagnetization energy term consideration, was performed. The obtained results present no variation relatively to the previous simulation making it clear that the exchange interaction is the only responsible for the coupling between inner magnetite core and maghemite shell.

With exception of the case $f = 0.65$, the obtained results for H_n follow the estimated tendency.

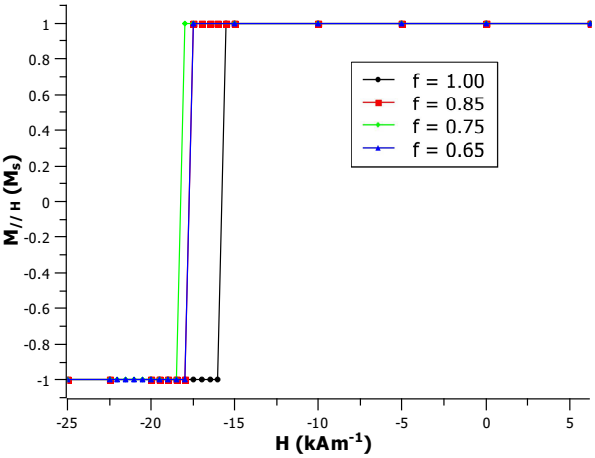

Figure 3.16: Hysteresis loops for the sphere of mixed composition.

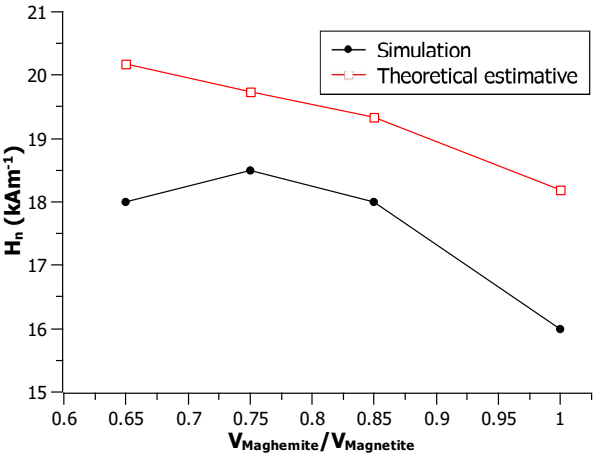

Figure 3.17: Variation of the nucleation field as function of the parameter f.

3.3.4 Volume Variation

For an uniformly magnetized ellipsoid of revolution, the demagnetization field is determined by the value of the axis ratios and is independent of their absolute values. As long as the single domain configuration is favoured, the energy density is given by the function 3.35 and so for the same axis ratios the nucleation field should not change. This insensitivity to volume variation may be used to verify the *MagPar* performance on the nucleation field determination. Following the procedure used on the composition variation study, the magnetization curves for one sphere with 10.0 *nm* radius and two spheres of radius 7.5 *nm* using different meshes. In order to find if the mesh used on the previous set

of simulations with sub-layers is the cause for the observed deviations it is necessary to compare it with a calculation using a mesh without layers. For that, the mesh generated for the compound core/shell structure was used for only magnetite and compared with a calculus with a simple mesh.

In Figure 3.18 the obtained magnetization curves and the curve obtained for $c/a = 1$ (in 'Geometry Variation') are plotted. The step used on field's variation implies an uncertain associated to the nucleation field of $1kA/m$, which covers the difference obtained between the spheres with $r = 7.5\ nm$ and $r = 10.0\ nm$ with the sphere with $r = 13.0\ nm$ but not the difference obtained for the mesh with sub-layers.

This deviation is attributed to the mesh distortion in the sub-layers that compose the shell. An anomaly in the total energy of this structure is found for the field value immediately before the reversal, as can be seen in Figure 3.19. The contribution of each energy term is plotted in Figure 3.20 showing that the biggest difference occurs in the exchange energy. A peak is also present on the E_{exch} curve for the mesh without shell structure, but the order of magnitude is much lower. It is clear that this peak is caused by small twists on the local magnetization sign of the magnetic configuration instability, small distortions that may promote the magnetization reversion process, lowering the value of H_n. It is not clear if these distortions are more likely to happen on the layered structure due to the smaller elements of the mesh, more sensible and appropriate do describe the process, or due to the geometrical distortion imposed on the shell mesh element.

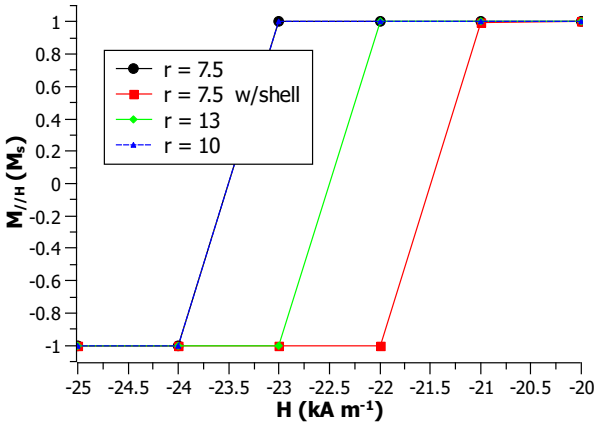

Figure 3.18: Hysteresis loops for spheres with different radius. There are 2 cases for radius 7.5 *nm* which differ on te mesh structure used, while one have the 'regular' mesh the other shares de mesh structure used in the spheres of mixed composition.

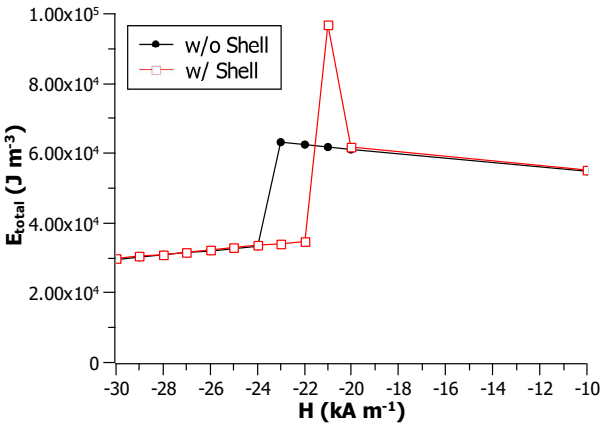

Figure 3.19: Comparison of the total energy variation with the applied field between the 2 sphere of $r = 7.5\ nm$ with different mesh structures.

3.4 Discussion

One characteristic factor, worth of analysis, of the hysteresis loops in Figures 3.9, 3.10 and 3.11 is their "squareness" (S) that is related with the coercive field slope [3] and can be defined as the ratio of the remanent magnetization (magnetization at $H = 0$) to M_s. For the considered nanoparticles it is not expected neither obtained a different magnetization at $H = 0$ than the saturated one, meaning that the traditional squareness definition can not be used. However a measure of squareness can be obtained as

$$S = 1 - \left| \frac{H_n - H_\alpha}{H_n} \right| \quad , \tag{3.39}$$

[3]The squareness factor is a dimensionless quantity between 0 and 1 which measures how square the loop is.

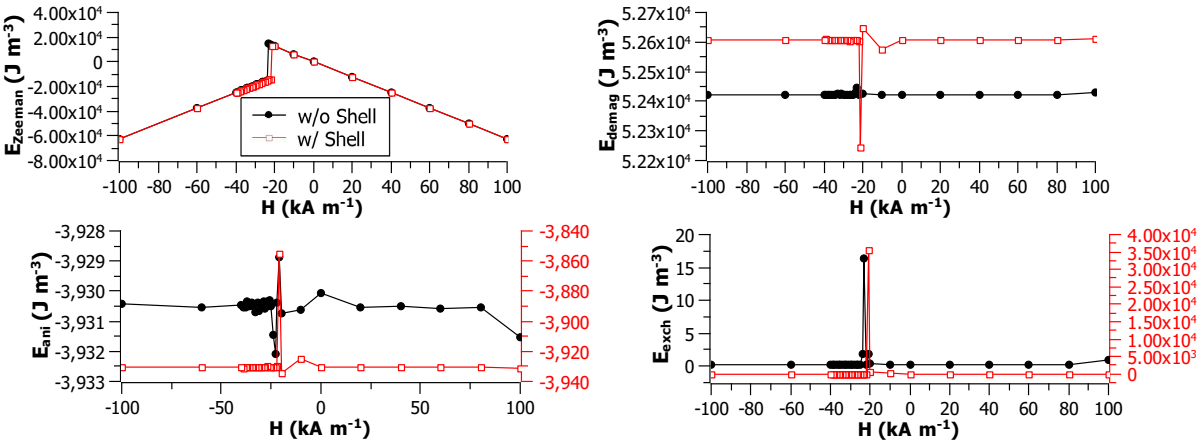

Figure 3.20: Comparison of each energy term contribution variation with the applied field between the 2 sphere of $r = 7.5\ nm$ with different mesh structures.

where H_α is the applied field for which the magnetization starts to invert, considered when the $M_{//H} < 0.99M_s$ condition was satisfied. In the classic Stoner-Wohlfarth model, a magnetic nanoparticle with its easy axis aligned along the magnetic field direction the has an hysteresis behaviour following perfect square with $S = 1$. Upon tilting the angle between the magnetic field and the easy axis to $\pi/2$, the hysteresis loop progressively close up and becomes fully closed ($S = 0$) when the angles reaches $\pi/2$. The obtained hysteresis loops and S values, on Table 3.3, contrast with the model previsions. Analysing in Figure 3.8 the deviation from the expected relaxed magnetization direction seems unlikely that the deviations, which would imply a non perfect alignment between applied field and magnetization easy axis, are responsible for the difference between model and results. Usually for work simplification, an uniaxial anisotropy is used in the classic Stoner-Wohlfarth model, while on these simulations the cubic magnetocrystalline anisotropy was considered along with a demagnetization field (from which the shape anisotropy arises) not aligned with an easy direction, resulting in their competition. Simulations results shown a tilt of the relaxed magnetization direction towards the magnetocrystalline easy axis as a result of the applied field interaction. This tilt is responsible for diminishing $M_{//H}$ up to the magnetization reversal which reduces the defined S value calculation. This effect increases when $c/a \to 1$, in agreement with the demagnetization energy and MAE magnitudes balance, the effect is clearer for the geometries with ratios 1.20 and 1.13. In these geometries, the magnetization direction rotation before the inversion can explain the divergence between the theoretical estimative of H_n and the obtained values, considering that in the theoretical approach the nucleation field was determined for the relaxed position.

For magnetic hyperthermia, the magnetic heat provided is proportional to the hysteresis loops enclosed area, that is proportional to the squareness. The squareness is then an important parameter to evaluate the nanoparticles performance. From the values in Table 3.3 it is possible do perceive that small uniaxial deformations on a spherical nanoparticle may lead to a significant loss in heating performance, and the use of elongated structures can be recommended since they are less susceptible to this problem.

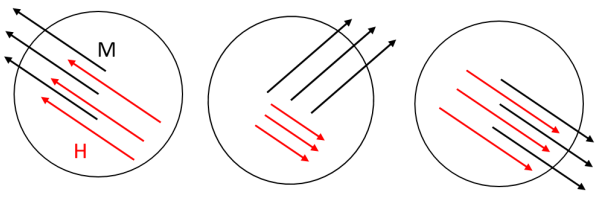

Figure 3.21: Scheme of the reversal mode obtained in some geometries, a coherent rotation between equivalent crystalline directions.

Table 3.3: Squareness values computed for the magnetite ellipsoids of revolution with different ratios c/a.

$\frac{c}{a}$	S
2.00	0.99
1.67	0.92
1.44	0.67
1.30	0.47
1.20	0.05
1.13	0.46
1.09	0.92
1.00	0.96
0.90	0.17
0.85	0.60

Usually the interest in using LLG equations on these kind of systems, is to study the reversal dynamics itself and not to determine the nucleation field. For all the simulated structures the reversal happened with a coherent rotation of the magnetization, however there was a difference between the structures with and without outer shell. While for the last ones the reversal happened essentially in discrete rotations between equivalent crystalline directions as illustrated in Figure 3.21, the former ones had a very different mode of rotation (yet still coherently). The simulations done for the magnetite spheres ($r = 7.5\ nm$) with and without the shell mesh structure have shown that the rotation mode obtained in the shell structures is caused by the used mesh and not by the system's physical properties.

By definition the nucleation field is the field at which the magnetization reversal initiates from the previously saturated state. From simulations data is difficult to set a criteria that may be used in all cases. Since for the non spherical ellipsoids the magnetization may be tilted from the relaxed position before the reversal takes place, a safe criteria would be the one used - the field at which the magnetization is reversed. The presence of peaks in the exchange energy was detected when comparing the two meshes used for the same system, however it was verified afterwards that these peaks are present in all the simulations effectuated. These peaks are caused by small distortions in the magnetization direction between neighbours nodes that happen right before or after a coherent rotation of the magnetization. In the obtained results for the hysteresis loops, exchange peaks associated with the tilting of the magnetization direction and peaks associated with the inversion can be identified. Comparing the field for the last exchange energy peak with the determined nucleation field, they coincide with an uncertainty of $\pm 1\ kAm^{-1}$ for the studied cases. Consequently, the identification of these peaks can help to determine the nucleation field in numerical simulations, or even be used as criteria for the nucleation in simulations with smaller field steps.

As observed in the results, the c/a ratio of the structure is a relevant parameter in the magnetization reversal, and relates to how strains/imperfections on the magnetic nanoparticles may affect the magnetic hyperthermia performance. As verified in the squareness measure, spherical nanoparticles may have their performance diminished by small strains/defects that either extend or compress the nanoparticle's shape, in Figure 3.12 this is made clear by the nucleation field for the sphere being a local maximum. Taking in account the squareness value that can be used to measure the reversal performance (the squarer the hysteresis loops, the better) and the nucleation field value, which is proportional to the dissipated heat through hysteresis cycles, the preferable choice for the magnetic nanoparticles shape is a prolate ellipsoid with c/a around 1.44, instead of sphere. For this ellipsoid the nucleation field is close to the

sphere, avoiding a high H_n which may be inconvenient for the clinical use of magnetic hyperthermia, and less sensible to small shape variations.

Due to the difference between magnetic properties of magnetite and maghemite, the nanoparticles oxidation could have a relevant impact on the magnetization reversal, although such situation was not verified in the obtained results. The nucleation field seems to have a small sensitivity to the compounds volume ratio, with higher H_n for a bigger volume of magnetite as expected. In fact between the half-magnetite half-maghemite case and the magnetite case, the nucleation field differs only by $6kAm^{-1}$, therefore the oxidation effects have a minor importance on the nanoparticles performance in magnetic hyperthermia.

An important computational aspect is the time spent by the simulations. The two longest simulations in the study of geometry variation and composition variation took approximately 4 and 8 weeks respectively. The difference between times is expected and it is caused by the much bigger number of mesh elements used to describe the outer shell in the mix composed spheres. However, in overall the studied structures are simple cases which does not justify the time taken. This might be an indication that the used parameter α (the dimensionless factor in LLG equation) might not be adequate for the used convergence criteria. The remaining simulations in the geometry variation study took around 2 days to complete the hysteresis loop suggesting that the α choice is the main responsible for the long simulation time. Then a test set must be carried out for an adequate choice of this numerical parameter.

Chapter 4

Conclusions and future work

The magnetic parameters M_s, K_1 and J for a magnetite crystal were determined using DFT and their dependence with the lattice parameter was studied through application of an uniaxial strain keeping volume constant. The study showed little sensitivity of the system to small strains, inducing no change of magnetic behaviour. Calculations with different Hubbard potentials were done to evaluate the LDA+U method performance of the parameters calculation, the potential $U_{eff} = 4.5$ being determined as the most suitable choice to have a better approximation of J. While the LDA+U method was necessary to compute the exchange constant (by allowing the system to converge to the ferromagnetic state) it seems to hinder the MAE calculation by diminishing its absolute value (in comparison with other calculations) that is already small for a crystal with cubic symmetry. Unfortunately, due to the limited numerical resources, it was not possible to determine K_1 and J for a maghemite crystal, only M_s. However using the obtained ion magnetic moments it was possible to estimate J for this material. The calculations performed for the magnetic parameters of a compound with an intermediate ratio of iron-oxygen atoms were unsuccessful, not allowing to study the parameters variation with the iron deficiency.

Complete hysteresis loops were simulated for magnetite ellipsoids of revolution with a c/a ratio ranging from 0.85 to 2.00, and half loops were simulated for spheres, with an outer shell of maghemite and a magnetite core, with volume ratio (Fe_3O_4/Fe_2O_3) ranging from 0.65 to 1.00. From the first results it was concluded that a shape of prolate ellipsoid with c/a ratio around 1.67 is preferable for these nanoparticles since it has a nucleation field similar to the sphere structure and its performance is less sensible to small deformations. The composed spheres allowed to determine that the oxidization effects on the nucleation field are small.

This project can be extended to simulate a distribution of nanoparticles randomly oriented to determine parameters as the remanent magnetization and the coercive field and compare both results and hysteresis loops with experimental data. Of course simulation of a considerable amount of particles with the mesh resolution used in this project represents a massive numerical effort and would require optimization of the computation. For the LLG relaxation, the realization of test sets to optimize the convergence criteria and the parameter α in the LLG equation can lead to a significant reduction of the simulation time.

Even thought thermal effects were not considered in this work, they have a major importance on magnetic hyperthermia since through thermal excitation the system can overcome the energy barrier(s) between states and in this way reverse the magnetization. The introduction of a stochastic field in the effective field definition is the method used generally to introduce thermal fluctuations in the LLG equation. Unfortunately the code *MagPar* does not support this option and this research would require another software. In that case, results from this work can be used as comparison for the $T = 0K$ case. A simpler

way to study the thermal activated reversal is to evaluate the energy barrier and use the *Néel* relaxation model as done by [30] [31].

Last but no least, it would be interesting to refine the technique used to generating the outer shell mesh in the spheres with mixed composition, since was shown that the used structure was not the most appropriate for the system. Reduction of the used layers to two or three and a gradual variation of element's sizes from the centre to the surface are ideas that seem to improve the mesh generation.

Bibliography

[1] S. Dutz and R. Hergt, "Magnetic particle hyperthermia - a promising tumour therapy?," *Nanotechnology*, vol. 25, no. 45, p. 452001, 2014.

[2] A. B. Salunkhe, V. M. Khot, and S. H. Pawar, "Magnetic hyperthermia with magnetic nanoparticles: a status review.," *Curr. Top. Med. Chem.*, vol. 14, no. 5, pp. 572–94, 2014.

[3] M. Carvalho, F. Henriques, L. Ferreira, M. Godinho, and M. Cruz, "Iron oxide nanoparticles: the influence of synthesis method and size on composition and magnetic properties," *J. Solid State Chem.*, vol. 201, pp. 144–152, 2013.

[4] S. Blundell, *Magnetism in Condensed Matter*. Oxford Master Series in Condensed Matter Physics 4, OUP Oxford, 2001.

[5] A. Aharoni, *Introduction to the Theory of Ferromagnetism*. International series of monographs on physics, Oxford University Press, 2000.

[6] H. Kronmuller, *Handbook of Magnetism and Advanced Magnetic Materials*. John Wiley & Sons, 2007.

[7] H. Eschrig, "The Fundamentals of Density Functional Theory (revised and extended version)," tech. rep., Institute for Solid State and Materials Research Dresden; University of Technology Dresden, 2003.

[8] E. R. Ylvisaker, W. E. Pickett, and K. Koepernik, "Anisotropy and magnetism in the LSDA + U method," *Phys. Rev. B*, vol. 79, p. 035103, jan 2009.

[9] K. Koepernik and H. Eschrig, "Full-potential nonorthogonal local-orbital minimum-basis band-structure scheme," *Phys. Rev. B*, vol. 59, pp. 1743–1757, Jan 1999.

[10] M. Richter, K. Koepernik, and H. Eschrig, "Full-potential local-orbital approach to the electronic structure of solids and molecules," *Condensed Matter Physics in the Prime of the 21st Century, Ed. J. Jedrzejewski, World Scientific, Singapore*, pp. 271–291, 2008.

[11] G. H. O. Daalderop, P. J. Kelly, and M. F. H. Schuurmans, "First-principles calculation of the magnetocrystalline anisotropy energy of iron, cobalt, and nickel," *Phys. Rev. B*, vol. 41, pp. 11919–11937, jun 1990.

[12] R. Řezníček, V. Chlan, H. Štěpánková, P. Novák, and M. Maryško, "Magnetocrystalline anisotropy of magnetite," *J. Phys. Condens. Matter*, vol. 24, p. 055501, feb 2012.

[13] J. P. Perdew, K. Burke, and M. Ernzerhof, "Generalized Gradient Approximation Made Simple," *Phys. Rev. Lett.*, vol. 77, pp. 3865–3868, oct 1996.

[14] D. J. Dunlop and Ö. Özdemir, *Rock Magnetism Fundamentals and Frontiers (Cambridge Studies in Magnetism)*. Cambridge University Press, 1997.

[15] K. Abe, Y. Miyamoto, and S. Chikazumi, "Magnetocrystalline Anisotropy of Low Temperature Phase of Magnetite," *J. Phys. Soc. Japan*, vol. 41, no. 6, pp. 1894–1902, 1976.

[16] M. Fleet, "The structure of magnetite," *Acta Crystallographica Section B: Structural Crystallography and Crystal Chemistry*, vol. 37, no. 4, pp. 917–920, 1981.

[17] H.-T. Jeng and G. Guo, "First-principles investigations of the electronic structure and magnetocrystalline anisotropy in strained magnetite Fe3O4," *Phys. Rev. B*, vol. 65, no. 9, pp. 1–9, 2002.

[18] E. Kroumova, J. Perez-Mato, and M. Aroyo, "Wycksplit: a computer program for determination of the relations of wyckoff positions for a group-subgroup pair," *Journal of Applied Crystallography*, vol. 31, no. 4, pp. 646–646, 1998.

[19] C. Pecharromán, T. González-Carreño, and J. E. Iglesias, "The infrared dielectric properties of maghemite, γ-Fe2O3, from reflectance measurement on pressed powders," *Phys. Chem. Miner.*, vol. 22, no. 1, pp. 21–29, 1995.

[20] A. Liechtenstein, V. Anisimov, and J. Zaanen, "Density-functional theory and strong interactions: Orbital ordering in mott-hubbard insulators," *Physical Review B*, vol. 52, no. 8, p. R5467, 1995.

[21] J. Wang, S.-H. Cao, W. Wu, and G.-m. Zhao, "The Curie temperature and exchange energy between two sublattices in half-metallic greigite Fe3S4," *ArXiv e-prints*, dec 2010.

[22] J. A. Osborn, "Demagnetizing Factors of the General Ellipsoid," *Phys. Rev.*, vol. 67, pp. 351–357, jun 1945.

[23] J. Fidler and T. Schrefl, "Micromagnetic modelling - the current state of the art," *J. Phys. D Appl. Phys*, vol. 33, no. 15, pp. 135–156, 2000.

[24] W. F. Brown, *Micromagnetics*. Interscience tracts on physics and astronomy, Interscience Publishers, 1963.

[25] L. Landau and E. Lifshitz, "On the theory of the dispersion of magnetic permeability in ferromagnetic bodies," *Phys. Z. Sowjetunion*, vol. 8, pp. 153–169, 1935.

[26] W. Scholz, J. Fidler, T. Schrefl, D. Suess, R. Dittrich, H. Forster, and V. Tsiantos, "Scalable parallel micromagnetic solvers for magnetic nanostructures," in *Comput. Mater. Sci.*, vol. 28, pp. 366–383, 2003.

[27] W. Scholz, "FrontPage - magpar wiki."

[28] U. Atxitia, P. Nieves, and O. Chubykalo-Fesenko, "Landau-Lifshitz-Bloch equation for ferrimagnetic materials," *Phys. Rev. B - Condens. Matter Mater. Phys.*, vol. 86, p. 104414, sep 2012.

[29] G. S. Abo, Y. K. Hong, J. Park, J. Lee, W. Lee, and B. C. Choi, "Definition of magnetic exchange length," *IEEE Trans. Magn.*, vol. 49, no. 8, pp. 4937–4939, 2013.

[30] J. Carrey, B. Mehdaoui, and M. Respaud, "Simple models for dynamic hysteresis loop calculations of magnetic single-domain nanoparticles: Application to magnetic hyperthermia optimization," *J. Appl. Phys.*, vol. 109, no. 8, p. 083921, 2011.

[31] J. García-Otero, A. García-Bastida, and J. Rivas, "Influence of temperature on the coercive field of non-interacting fine magnetic particles," *J. Magn. Magn. Mater.*, vol. 189, no. 3, pp. 377–383, 1998.

[32] B. D. Cullity and C. D. Graham, *Introduction to Magnetic Materials*. Hoboken, NJ, USA: John Wiley & Sons, Inc., 2nd ed., 2008.

Appendix

Theoretical calculations for uniform ellipsoids of revolution

Parameters

```
μ0 = 4 π * 10^(-7); μB = 9.27 * 10^(-24);
K1 = -1.17919 * 10^4; M = 7.9978386 / 2;
V = (8.3941 * 10^(-10))^3 ; Ms = 8 * μB M / V ;
```

Prolate Ellipsoid

Demagnetization Factors

```
p = {2, 1.67, 1.44, 1.30, 1.20, 1.13, 1.09} ;
ξ = Sqrt[p^2 - 1] / p;
Dz = (1 / (p^2 - 1)) * (Log[(1 + ξ) / (1 - ξ)] / (2 ξ) - 1); Dx = (1 - Dz) / 2;
```

Energy Variation (no field):

```
Eprolate[x_] := K1 (Sin[x]^2 (0.25 Sin[x]^2 + Cos[x]^2)) +
  μ0 Ms^2 (Dx * Sin[x]^2 + Dz * Cos[x]^2) / 2
```

Relaxed Angle

```
x0 = Table[x /. Last[FindMinimum[Eprolate[x][[i]], {x, 0.6}]], {i, 1, 7, 1}]
```

$$\{-2.58\times10^{-13},\ 2.26301\times10^{-11},\ 1.04371\times10^{-14},\ 5.10001\times10^{-10},\ 0.18627,\ 0.509977,\ 0.646436\}$$

First and Second Derivatives

```
DEprolate[x_, H_] :=
 (-1.5 K1 Cos[x] Sin[x]^3 + 1/2 Ms^2 μ0 (2 Dx Cos[x] Sin[x] - 2 Dz Cos[x] Sin[x]) +
    2 K1 Cos[x] Sin[x] (Cos[x]^2 + 0.25 Sin[x]^2)) + μ0 H Ms Sin[x - x0]

D2Eprolate[x_, H_] :=
 (-6. K1 Cos[x]^2 Sin[x]^2 + K1 (2 Cos[x]^2 - 2 Sin[x]^2) (Cos[x]^2 + 0.25` Sin[x]^2) +
    K1 Sin[x]^2 (-2 Cos[x]^2 + 2 Sin[x]^2 + 0.25` (2 Cos[x]^2 - 2 Sin[x]^2)) + 1/2 Ms^2 μ0
     (Dx (2 Cos[x]^2 - 2 Sin[x]^2) + Dz (-2 Cos[x]^2 + 2 Sin[x]^2))) + μ0 H Ms Cos[x - x0]
```

Nucleation field

```
Tol = 10^(-4);  Step = Pi / 50;
For[ii = 1, ii ≤ 7, ii++,
          jj = {Null};
                x = x0[[ii]]
                For[H = -100 000, H ≤ 0, H = H + 10,
                 AppendTo[jj, If[Abs[DEprolate[x0[[ii]], H][[ii]]] ≤ Tol &&
          D2Eprolate[x0[[ii]], H][[ii]] ≤ Tol, H]];
    ]
             jj = DeleteCases[jj , Null]; jj = DeleteCases[jj , 0]; Print[Max[jj]]
      ]
```

```
-82 740
-55 680
-31 060
-12 900
-3720
-20 390
-25 960
```

Sphere

```
Esphere[x_, H_] :=
 K1 (Sin[x]^2 (0.25 Sin[x]^2 + Cos[x]^2)) - μ0 H Ms Cos[x - ArcTan[Sqrt[2]]]

Plot[K1 (Sin[x]^2 (0.25 Sin[x]^2 + Cos[x]^2))
```

First and Second Derivatives

```
DEsphere[x_, H_] := -1.5 K1 Cos[x] Sin[x]^3 +
   2 K1 Cos[x] Sin[x] (Cos[x]^2 + 0.25 Sin[x]^2) + μ0 H Ms Sin[x - ArcTan[Sqrt[2]]]

D2Esphere[x_, H_] :=
 (-6. K1 Cos[x]^2 Sin[x]^2 + K1 (2 Cos[x]^2 - 2 Sin[x]^2) (Cos[x]^2 + 0.25 Sin[x]^2) +
    K1 Sin[x]^2 (-2 Cos[x]^2 + 2 Sin[x]^2 + 0.25` (2 Cos[x]^2 - 2 Sin[x]^2))) +
  μ0 H Ms Cos[x - ArcTan[Sqrt[2]]]
```

Nucleation field

```
jj = {Null};  Tol = 10^(-3);  Step = Pi / 100;
For[x = ArcTan[Sqrt[2]], x ≤ 2 Pi, x = x + Step,
 For[H = -100 000, H ≤ 0, H = H + 100,

  AppendTo[jj, If[Abs[DEsphere[x, H]] ≤ Tol && D2Esphere[x, H] < Tol, H]]
          ]
]
        jj = DeleteCases[jj , Null]; jj = DeleteCases[jj, 0]; Max[jj]
```

```
-25 000
```

```
(4 / 3) K1 / (Ms μ0)
```

```
-24 953.
```

Oblate Ellipsoid

Demagnetization Factors

```
q = 1 / {0.9, 0.85};
dz = q^2 / (q^2 - 1) (1 - 1 / Sqrt[q^2 - 1] ArcSin[Sqrt[q^2 - 1] / q]);
dx = (1 - dz) / 2;

Eoblate[x_] := K1 (Sin[x]^2 (0.25 Sin[x]^2 + Cos[x]^2)) +
  μ0 Ms^2 (dx * Sin[x]^2 + dz * Cos[x]^2) / 2
```

Relaxed Angle

```
x0 = Table[x /. Last[FindMinimum[Eoblate[x][[i]], {x, 0.6}]], {i, 1, 2, 1}]
```

```
{1.5708, 1.5708}
```

First and Second Derivatives

```
DEoblate[x_, H_] :=
  (-1.5 K1 Cos[x] Sin[x]^3 + 1/2 Ms^2 μ0 (2 dx Cos[x] Sin[x] - 2 dz Cos[x] Sin[x]) +
     2 K1 Cos[x] Sin[x] (Cos[x]^2 + 0.25 Sin[x]^2)) + μ0 H Ms Sin[x - x0]

D2Eoblate[x_, H_] :=
  (-6. K1 Cos[x]^2 Sin[x]^2 + K1 (2 Cos[x]^2 - 2 Sin[x]^2) (Cos[x]^2 + 0.25` Sin[x]^2) +
     K1 Sin[x]^2 (-2 Cos[x]^2 + 2 Sin[x]^2 + 0.25` (2 Cos[x]^2 - 2 Sin[x]^2)) + 1/2 Ms^2 μ0
      (dx (2 Cos[x]^2 - 2 Sin[x]^2) + dz (-2 Cos[x]^2 + 2 Sin[x]^2))) + μ0 H Ms Cos[x - x0]
```

Nucleation field

```
Tol = 10^(-4); Step = Pi / 50;
For[ii = 1, ii ≤ 2, ii++,
          jj = {Null};
              For[H = -50 000, H ≤ 0, H = H + 10,
                 AppendTo[jj, If[Abs[DEoblate[x0[[ii]], H][[ii]]] ≤ Tol &&
          D2Eoblate[x0[[ii]], H][[ii]] < Tol, H]];
               ]
            jj = DeleteCases[jj , Null]; Print[Max[jj]]
      ]
```

```
-2720
```

```
-14 560
```